Chapter 13
Mechanical and Electrical Principles for Separation of Rare Cells

Elisa M. Wasson, Temple A. Douglas, and Rafael V. Davalos

Abstract Early detection of disease has long been a goal of many research projects and public health initiatives, as prevention from disease advancement is one of the most effective cures. Many diseases that are difficult to treat in late stage such as melanoma, pancreatic cancer, and highly metastatic tumors are treatable with a much better prognosis in early stage. One method of interest in early cancer detection has been the isolation of circulating tumor cells (CTCs) from the blood. By isolating CTCs, we can determine the presence of cancer from only a blood sample rather than requiring multiple screening modalities be performed on a patient. In addition, cancers without effective screening modalities, such as pancreatic cancer, may produce CTCs while the patient is asymptomatic, allowing for a much earlier start to treatment and improved prognosis [1]. In this chapter, we present several approaches that employ microfluidics to separate rare cells of interest. We start with a basic overview of fluid dynamics that includes scaling analysis and several solutions to the Navier-Stokes equations. We then introduce mechanical and electrical separation techniques along with an overview of their respective theories and several examples of each.

Keywords Inertial microfluidics • Dielectrophoresis • DEP • Circulating tumor cells (CTCs)

13.1 Introduction and Brief Description of Chapter

Early detection of disease has long been a goal of many research projects and public health initiatives, as prevention from disease advancement is one of the most effective cures. Many diseases that are difficult to treat in late stage such as

E.M. Wasson (✉) • T.A. Douglas • R.V. Davalos, Ph.D.
Bioelectromechanical Systems Lab, Department of Mechanical Engineering, Virginia Tech—Wake Forest University, School of Biomedical Engineering and Sciences, 330 Kelly Hall (MC0298), Blacksburg, VA 24061, USA
e-mail: ewasson1@vt.edu; tadougla@vt.edu; davalos@vt.edu

C. Lu, S.S. Verbridge (eds.), *Microfluidic Methods for Molecular Biology*,
DOI 10.1007/978-3-319-30019-1_13

melanoma, pancreatic cancer, and highly metastatic tumors are treatable with a much better prognosis in early stage. One method of interest in early cancer detection has been the isolation of circulating tumor cells (CTCs) from the blood. By isolating CTCs, we can determine the presence of cancer from only a blood sample rather than requiring multiple screening modalities be performed on a patient. In addition, cancers without effective screening modalities such as pancreatic cancer may produce CTCs while the patient is asymptomatic, allowing for much earlier start to treatment and improved prognosis [1].

One of the key challenges in isolating CTCs is their rarity. The presence of CTCs in the blood is thought to be at concentration 1–10 cells in 10 mL of whole blood [2]. Without some method to specifically isolate these cells from a sample, their low concentrations make them almost impossible to detect. While many successful microfluidic devices use biomarker-specific analysis to detect the presence of cancer, the focus of this chapter will be microfluidic techniques that provide label-free isolation and enrichment with high cell viability, allowing them to be cultured for further analysis and potential targeted treatment.

This chapter focuses on the isolation of rare mammalian cells as opposed to viruses and bacteria. First, a brief overview of microfluidic theory will be given including scaling laws, several analytical solutions to the Navier-Stokes equations, dimensionless parameters used in microfluidics, as well as Stokes law and drag force. Next, particle dynamics will be discussed using a force balance approach for both passive and active methods. Mechanical (passive) and electrical (active) methods of separation will be discussed in depth, giving several examples and their limitations for each technique. Implications for the future of microfluidic technologies to separate rare cell populations are also discussed.

13.2 Basic Physics in Microfluidics

Microfluidic devices allow researchers to replicate conditions found inside the body in order to investigate mammalian cells in their natural environment. Devices typically have length scales and dimensions that are comparable to fluid flow systems in the body such as arteries (0.1–10 mm), alveoli in the lungs (200 μm), as well as sinusoids (30–40 μm) and lobules in the liver (500–1000 μm). Parameters such as geometry, shear stress, flow rate, oxygen concentration, and pulsatile flow can be precisely controlled and modified to replicate conditions found in vivo using an in vitro platform. These capabilities of microfluidic devices give researchers the power to investigate the cell's role in diseases such as cancer [3–5], malaria [6–8], and HIV [9–11]. Microfluidic devices can also take advantage of physical phenomena that occur at the microscale, lending to cell separation techniques that have the potential to lower the cost, time, resources, reagents, and lab infrastructure necessary to operate many of the current clinical separation technologies [12–16].

Therefore, when separating and analyzing mammalian cells using microfluidic devices, it is necessary to have a firm grasp of the physics and forces that dominate at the microscale.

13.2.1 The Continuum Hypothesis

Particle spacing and scale play an important role in determining how to model a fluidic system. Consideration should be given to what physics must be captured in order to scale the system accordingly. It is important to choose the relevant characteristic length scale that describes the phenomena of interest within the system. For example, if you are interested in particle dynamics, the diameter of the particle may serve as the best characteristic length. On the other hand, if you are interested in the fluid flow in a microfluidic device, the channel diameter should be chosen as the characteristic length. The physics of a system may have different influence at varying scales. If there is a nanofluidic channel with a characteristic length scale defined as the channel diameter, on the order of a few nanometers, the particles in the fluid experience forces differently than particles in a flowing river with a characteristic length scale defined as the width, in kilometers. Intermolecular forces, such as van der Waals attraction and Brownian motion, influence the flow in a way that can be considered negligible in the flowing river. This difference is due to the continuum assumption, which is defined using the dimensionless Knudsen number:

$$K_n = \frac{\lambda}{L} \tag{13.1}$$

For microfluidics, the Knudsen number is the ratio between the intermolecular distance of water (λ) and the characteristic length scale of the system (L) which is usually the diameter of the device channel. If $K_n < 0.01$, the continuum hypothesis is valid [17]. Water has an intermolecular distance of 0.3 nm [18], meaning that a water molecule must travel this distance before colliding with its neighbor. Therefore, if the characteristic length scale is on the same order as the intermolecular distance, like the nanofluidic channel, the fluid can no longer be considered continuous and there may be a point in the fluid that does not have a finite value defined for properties such as density and velocity. These physical properties are then considered discontinuous and the continuum assumption breaks down. On the contrary, if the characteristic length scale of the system is much larger than that of the particle spacing, it can be assumed that the fluid is continuous and all physical properties are averaged over many molecules. While the elements of fluid being analyzed are large enough to consider mean representations of molecular effects, they are also small enough to allow them to still be considered differential elements. This allows for spatial and temporal variations of fluid properties to be investigated using continuum mechanics. Microfluidic devices are typically tens to hundreds of

Table 13.1 Knudsen values for different flow regimes

$K_n < 0.01$	Continuum model, non-slip flow
$0.01 \leq K_n < 1$	Continuum model, slip-flow
$1 \leq K_n < 10$	Transition region
$K_n \geq 10$	Free-molecular region

microns in size resulting in $K_n \ll 0.01$ allowing continuum mechanics to be used. A nanofluidic device, on the other hand, with a diameter of 10 nm will have a Knudsen number of 0.3 which is greater than 0.01. This leads to slip-flow where the molecules of the fluid may collide with channel walls before they interact with each other, therefore inducing discontinuities in properties (i.e., density, velocity) at the fluid-solid surface.

Systems with a Knudsen number higher than one no longer satisfy the continuum assumption. At this scale, complex collisions occur and intermolecular forces between particles must be considered. In order to analyze a non-continuum system, deterministic or statistical molecular models must be used which require extensive computational resources [19–21]. Non-continuum models are complicated and difficult to solve whereas continuum is not only easier to compute, but well characterized and more predictable [17]. As summarized in Table 13.1, the Knudsen number, along with several other parameters discussed in a later section, can be a powerful tool in classifying the flow of the system and determining the correct modeling approach needed to solve the problem. Depending on the scale of the system, the relevant physics at each regime will vary, demanding a closer look at the effects scaling can have in microfluidics.

13.2.2 Scaling Laws

As demonstrated by the continuum hypothesis, taking a macroscopic approach to define a system can lead to a drastically different outcome than applying a microscopic approach to an identical system. This is apparent when administering drugs to patients of different sizes. A man who is 6 feet tall and weighs 200 lb is typically going to need a larger dose of the same drug than that of a small boy who weighs 70 lb. This is due to differences in their size and metabolism. The same is true for other physical phenomena. At the macroscale, volumetric forces such as gravity and inertia typically dominate the physics that occur on a day-to-day basis. If we were to apply these macroscopic principles to objects at the microscale, it will lead to detrimental errors in our calculations. In order to avoid this, it is necessary to develop a method to scale physical parameters and gain a more accurate understanding. This is known as scaling analysis and can be classified as either geometric or dynamic [22].

13.2.2.1 Geometric Scaling

Geometric scaling relates directly to the size of an object. Table 13.2 lists scaling laws for length, area, volume, weight, and mass. Despite the simplicity of these laws, they provide immense insight for dynamic systems involving rules that are more complex.

One example of geometric scaling is to compare a human to the Brazilian pygmy gecko. This 4 cm long reptile resides in the Amazon jungle, and in order to survive the large amount of rainfall, has adapted to its climate by developing the ability to float on water while standing. Its small stature and hydrophobic skin help to repel water and prevent its body from breaking the surface tension of puddles on the jungle floor [23]. If we approximate the small gecko with a cube having a side length of 4 cm, we can calculate both its surface area and volume to be 96 cm^2 and 64 cm^3, respectively. The ratio of its surface area to volume is found to be 1.5. This is obviously oversimplifying the analysis, but for demonstrating purposes shows how drastically size can affect the behavior of an object at different scales. If a human attempts to walk on water, the outcome is not as favorable as that of the gecko. This is due to the fact that an average male who is 170 cm tall has a surface area-to-volume ratio of 0.035. In order for a person to have a chance of walking on water, they would need to have a surface area 42 times larger than what it currently is. From Table 13.2, we can see that surface area is a second-order scaling law whereas volume is a third-order law. If the length of the man were to double, his surface area would quadruple and his volume would octuple. Therefore, for larger objects, volume will always increase faster than surface area and lead to a smaller ratio of the two. At the microscale, the surface area-to-volume ratio is large and hence surface forces and effects dominate over volumetric forces. Sometimes it is useful to create a visual representation of scaling parameters in order to gain an intuition for how small objects will behave. Figure 13.1 shows the surface area-to-volume ratio for a cell, the nematode *Caenorhabditis elegans* (*C. elegans*), the Brazilian pygmy gecko, and an average-sized man.

As described previously, the pygmy gecko has a surface area-to-volume ratio 42 times larger than the average-sized man, therefore making it possible for it to stand on water without sinking. The adult nematode, *C. elegans*, is on average 1 mm long and has a surface area-to-volume ratio of 60. This nematode is capable of swimming in highly viscous fluids due to its small size and the undulations it undertakes to propel itself forward. Finally, a single cell with an average diameter of 10 μm has a surface area-to-volume ratio of 6000! Clearly, a single cell experiences forces differently than an average-sized man at the macroscale. Scaling laws of these different forces are discussed in the next section to understand just how much of an influence macroscale forces have at the microscale.

Table 13.2 Geometric scaling laws

Name	Formula	Order
Length (L)	$L \sim l^1$	1
Area (A)	$A \sim l^2$	2
Volume/weight/mass (V)	$V \sim l^3$	3

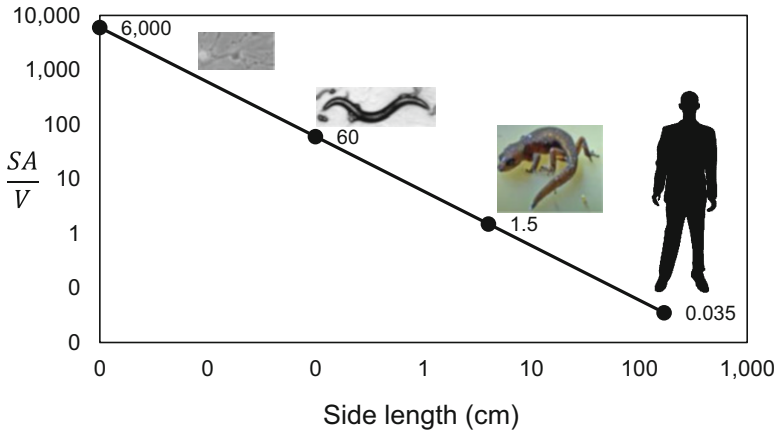

Fig. 13.1 Surface area-to-volume ratio for different organisms

13.2.2.2 Dynamic Scaling

In dynamic scaling, the laws of motion come into play and forces need to be scaled in order to understand their behavior at the microscale. Starting with Newton's second law, we can determine the scaling laws for both the acceleration of an object (a) and the time (t) it takes to get from point A to B in terms of force (F), mass (m), and length scale (l) [24]. Based on Newton's second law:

$$a = \frac{F}{m} \sim Fl^{-3} \tag{13.2}$$

Taking this a step further to determine the scaling law for the time (t) it takes an object to move from one point to another, we can denote displacement as l and use the following kinematic equation:

$$l = v_o t + \frac{1}{2} a t^2 \tag{13.3}$$

Assuming that initial velocity, v_o, is equal to zero, we are left with an equation for time:

$$t = \left(\frac{2l}{a}\right)^{0.5} \sim l^2 \, F^{-0.5} \tag{13.4}$$

Depending on the force causing motion of the object, time and acceleration will scale differently. Table 13.3 summarizes the scaling laws for various forces and parameters that play a key role in microfluidics. For example, if we were interested in the effect a volumetric force, such as gravity, $\left(F_g = \rho V g\right)$ has on the time it takes

Table 13.3 Dynamic scaling laws

Name	Formula	Variables	Scaling	Order
Gravity/inertia	V	V—volumetric force	l^3	3
Surface tension	$F = 2\pi\sigma r$	σ—surface tension r—contact radius	l^1	1
Reynolds number	$Re = \frac{\rho VD}{\eta}$	ρ—density V—velocity D—diameter η—dynamic viscosity	l^2	2
Viscous forces	$F = A\eta\frac{du}{dx}$	A—area η—viscosity dx—distance from body u—velocity	l^{1+u}	$1+u$
Magnetic force	$F = iL\mu_0\left(\frac{n}{L}\right)i$	i—current L—length of wire n—# turns in wire μ_0—permeability	l^4	4
Kinetic energy	$F = \frac{1}{2}mv^2$	m—Mass ν—velocity	l^3	3
Resistance	$R = \rho\frac{L}{A}$	ρ—density L—length A—area	l^{-1}	-1
Capacitance	$C = \varepsilon\frac{A}{x}$	A—area ε—permittivity x—distance between source and ground	l^1	1
Electric field	$E = \frac{V}{x}$	V—electric potential x—distance between source and ground	l^{-1}	-1
Electrostatic	$F = \frac{\varepsilon_o A(\Delta V)^2}{2d^2}$	A—area ΔV—potential d—distance between source and ground ε_o—permittivity of free space	l^2	2

an object to move from one place to another, force would scale as l^3 and time would scale as $l^{0.5}$. Most forces tend to scale as order two; therefore microscale objects tend to accelerate faster than macroscale objects [24]. As objects become smaller $(l \downarrow)$, the time it takes for them to get from one point to another also decreases. For a force that scales as second order, the object will have a time scale of the first order. Therefore, if one object is ten times larger than another object, it will take ten times as long to travel from one point to another.

It is important to keep in mind that these scaling laws can be applied using the length scale of the particle being investigated, or as an alternative may be applied using the characteristic length of the channel itself. When using scaling analysis, it is necessary to be aware of the physics you are interested in capturing, what is being scaled, and then scale the system accordingly. As a result, the scaling laws found in Table 13.3 may vary slightly depending on what is being scaled.

13.2.3 Fluid Dynamics

13.2.3.1 Navier-Stokes Equations

Since most microfluidic devices have a Knudsen number less than 0.01, continuum mechanics may be used and the Navier-Stokes equations become the governing equations. The Navier-Stokes equations consist of three nonlinear, partial differential equations with five unknown parameters where the velocity vector is denoted by $\vec{u}$ and has xyz components, p is pressure, and ρ is density. The constants g and η are defined as gravity and dynamic viscosity, respectively. In order to solve for all of the parameters, we need a fifth equation to fully define the system. We can assume that the flow is incompressible and therefore define density, ρ, to be constant, making it spatially uniform. This fifth equation of state, along with conservation of momentum (continuity), now provides a complete description of fluid flow for incompressible, Newtonian fluids.

Mass conservation (continuity):

$$\nabla \cdot \vec{u} = 0 \tag{13.5}$$

Navier-Stokes:

$$\rho \frac{\partial \vec{u}}{\partial t} + \rho \vec{u} \cdot \nabla \vec{u} = -\nabla p + \eta \nabla^2 \vec{u} + \rho \vec{g} \tag{13.6}$$

The first term in the Navier-Stokes equations is the unsteady, local inertial term. The second term is the convective inertial term and is responsible for nonlinear behavior in the fluid flow. The right-hand side of Eq. (13.6) contains both body forces (gravity) and surface forces (shear stress and pressure) of the fluid. It is possible to solve the Navier-Stokes equations analytically for different conditions by making some basic assumptions about the flow or geometry of the system and applying the no-slip boundary condition.

No-slip boundary:

$$\vec{u} = 0 \tag{13.7}$$

This equation states that the velocity of the fluid at a motionless wall is zero. This holds true for most devices at the microscale because the length scale of the system is generally larger than the intermolecular spacing and continuum applies. In the following section, we discuss the solutions for different geometries that are common in microfluidic devices.

13.2.3.2 Analytical Solutions for Different Geometries

Most microfluidic channels have cross-sectional areas that are either circular or rectangular due to photolithography and etching techniques used to fabricate the devices. Solutions to the Navier-Stokes equations for these two geometries can be found analytically using integration or through series expansion methods. As seen in Table 13.4, a channel with a circular cross section of radius R is often approximated as a cylindrical tube with length L and its velocity equation is solved for analytically using cylindrical coordinates. The Navier-Stokes equations in cylindrical coordinates can be found in Munson, Young Okiishi, and Huebsch's "Fundamentals of Fluid Mechanics" [25]. Assuming steady, incompressible, laminar, fully developed, and axially symmetric flow and applying the no-slip and symmetry boundary conditions lead to the following equation that describes the velocity profile.

Velocity profile (cylinder):

$$u_z(r) = \frac{1}{4\eta}\frac{\partial p}{\partial z}\left(r^2 - R^2\right) \tag{13.8}$$

Here pressure is defined as p and η is the viscosity of the fluid. We can also define the pressure gradient and calculate flow rate by integrating the velocity over the differential area. Note that the pressure gradient is negative because pressure decreases in the direction of flow.

Pressure drop (cylinder):

$$-\frac{\partial p}{\partial z} = \frac{\Delta p}{L} \tag{13.9}$$

Volumetric flow rate (cylinder):

$$Q = \int_0^R u_z(r)\, dA = 2\pi \int_0^R u_z(r)\, r dr = \frac{\pi R^4 \Delta p}{8\eta L} \tag{13.10}$$

This results in the familiar Hagen-Poiseuille equation whose step-by-step derivation can be found in Munson's "Fundamental Fluid Mechanics" [25]. We can see that for a given pressure drop, flow rate scales as l^4 since the flow rate is proportional to the radius to the fourth power. As a channel gets smaller, the flow rate will decrease drastically, therefore making it difficult to drive fluids in microchannels using conventional pressure drop methods. High pressures are necessary to obtain high flow rates due to the fluidic resistance of the channels. Table 13.4 summarizes the resistance of different shaped cross-section microchannels which can be determined using an analogous form of Ohm's law. In this equation, voltage is represented by pressure drop (Δp), current is represented by flowrate (Q), and resistance (R) is defined as fluidic resistance. Techniques such as electrokinetic

Table 13.4 Flow conditions for various channel geometries

	Parallel plate	Cylindrical	Rectangular
Geometry	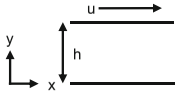	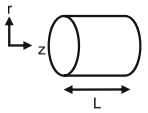	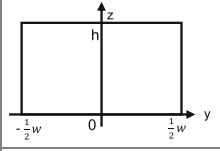
Velocity profile	$u_x(y) = \frac{h^2}{2\mu}\frac{\Delta p}{L}\left[\left(\frac{y}{h}\right) - \left(\frac{y}{h}\right)^2\right]$	$u_z(r) = \frac{1}{4\eta}\frac{\Delta p}{L}\left(R^2 - r^2\right)$	$u_x(y,z) = \frac{4h^2\Delta p}{\pi^3\eta L}\sum_{n,\text{odd}}^{\infty}\frac{1}{n^3}\left[1 - \frac{\cosh\left(n\pi\frac{y}{h}\right)}{\cosh\left(n\pi\frac{w}{2h}\right)}\right]\sin\left(n\pi\frac{z}{h}\right)$
Flow rate	$Q = \frac{h^3\Delta p}{12\eta L}$	$Q = \frac{\pi R^4\Delta p}{8\eta L}$	$Q = \frac{h^3 w\Delta p}{12\eta L}\left[1 - 0.630\frac{h}{w}\right]$
Fluidic resistance	$R_h = \frac{12\eta L}{h^3}$	$R_h = \frac{8\eta L}{\pi R^4}$	$R_h = \frac{12\eta L}{(1 - 0.63)\left(\frac{h}{w}\right)h^3 w}$

flow where fluid is driven by the movement of molecules in an electric field either by electroosmosis and electrophoresis are commonly used in microfluidic devices for this reason [26].

Due to standard fabrication techniques, many microchannels are not circular but instead have a rectangular cross-sectional area with width w and height h. The solution for a rectangular channel is a bit more involved than a circular channel because it is a two-dimensional, elliptic partial differential equation. Therefore, integration cannot be used to solve directly for the velocity profile, but instead a Fourier series expansion is used. Assuming steady, laminar, fully developed, and incompressible flow leads to a reduced form of the Navier-Stokes equations. Performing a Fourier series expansion and applying the no-slip boundary conditions at each surface yield the equation for the velocity profile derived in full by Bruus' "Theoretical Microfluidics" [18].

Velocity profile (rectangular):

$$u_x(y,z) = \frac{4h^2\Delta p}{\pi^3 \eta L} \sum_{n,\,\text{odd}}^{\infty} \frac{1}{n^3} \left[1 - \frac{\cosh\left(n\pi\frac{y}{h}\right)}{\cosh\left(n\pi\frac{w}{2h}\right)}\right] \sin\left(n\pi\frac{z}{h}\right) \tag{13.11}$$

In order to find an equation for the flow rate, we need to integrate the velocity equation over the area of the channel. This results in a complicated solution, but we are able to simplify this even further by assuming that our channel is going to be very wide and flat where the width is much larger than the height $\left(\frac{h}{w} \to 0\right)$ [18].

Flow rate (rectangular):

$$Q \approx \frac{h^3 w \Delta p}{12\eta L}\left[1 - 0.630\frac{h}{w}\right] \tag{13.12}$$

Flow in a microchannel can also be approximated as a 2D flow where we can model the channel walls as two infinitely long parallel plates with a height, h, separating them. In this instance, we have pressure-driven flow and consider the same assumptions. Flow is steady, incompressible, fully developed, and laminar, therefore reducing the Navier-Stokes equations significantly and leaving a balance between pressure and shear stress. Solving through integration and applying the no-slip boundary condition [25] at the top $(y = h)$ and bottom walls $(y = 0)$, we can obtain the equation for the velocity profile, flow rate, and pressure drop in the channel.

Velocity profile (parallel plate):

$$u_x(y) = \frac{h^2}{2\mu}\frac{dp}{dx}\left[\left(\frac{y}{h}\right)^2 - \left(\frac{y}{h}\right)\right] \tag{13.13}$$

Pressure drop (parallel plate):

$$-\frac{dp}{dx} = \frac{\Delta p}{L} \tag{13.14}$$

Flow rate (parallel plate):

$$Q = \frac{h^3 \Delta p}{12 \eta L} \tag{13.15}$$

Table 13.4 summarizes the results found by solving the Navier-Stokes equations for a cylinder, rectangular, and parallel plate channel. The geometry of the system is defined as well as the velocity profile, flow rate, and fluidic resistance equations.

13.2.3.3 Nondimensionalization and Stokes Flow

In order to gain a better understanding of the Navier-Stokes equation and deduce which forces become important at the microscale, it is necessary to nondimensionalize the equation. As with any engineering system, nondimensionalization provides a method to gain a better intuition for what is happening in the system. If viscous forces are large, how large are they? In relation to what? These are all questions that can be answered by taking a nondimensional approach. To start our nondimensionalization, we need to pick characteristic values in order to form the correct dimensionless variables, which will be represented with an asterisk.

Here, we choose a length scale of l to nondimensionalize our spatial variables, a characteristic velocity, U, to nondimensionalize our velocity terms and a time that scales as velocity over distance $\left(t^* = \frac{tU}{l}\right)$. We choose to use viscous pressure $\left(p^* = \frac{pl}{\eta U}\right)$ instead of dynamic pressure $\left(p = \frac{P}{\rho U^2}\right)$ since, through our scale analysis, we have determined that inertial forces will become negligible at small scales in comparison to viscous forces which will dominate [27, 28]. For this reason, we also assume that body forces such as gravity are negligible. If we were to choose dynamic pressure and follow through with the nondimensionalization, the pressure term will be eliminated from the equation. Yet we know that pressure does in fact play a role at the microscale and this would result in an inaccurate solution. Substituting these dimensionless variables into the Navier-Stokes equations and simplifying gives the following equation:

$$Re_c * \left(\frac{\partial \vec{u}^*}{\partial t^*} + \vec{u}^* \cdot \nabla^* \vec{u}^* \right) = - \nabla^* p^* + \nabla^{*2} \vec{u}^* \tag{13.16}$$

The dimensionless number that is present, Re_c, is the channel Reynolds number and is one of the most widely used parameters in the microfluidics field. The channel Reynolds number is the ratio of inertial forces to viscous forces and is defined as

$$Re_c = \frac{\text{inertial forces}}{\text{viscous forces}} = \frac{\rho U l}{\eta} = \frac{\rho U D_h}{\eta} \tag{13.17}$$

where l is the characteristic length and is usually defined as the hydraulic diameter of the channel which is dependent on area, A, and perimeter, P $\left(D_h = \frac{4A}{P}\right)$, when analyzing fluid flow. Since microfluidic devices have relatively small diameters (10–100 μm) and low velocities (1 μm/s–1 cm/s), the Reynolds number is typically between 10^{-4} and 1 for most devices, making the majority of flow laminar and viscous dominated [29]. In this case, it is possible to simplify the governing equation even further. Taking the limit of Reynolds number as it approaches zero results in the following simplified momentum equations in three dimensions:

$$0 = -\nabla^* p^* + \nabla^{*2} \vec{u}^* \tag{13.18}$$

This is known as Stokes flow for low Reynolds number ($Re_c \ll 1$). The governing equation has been simplified greatly, eliminating the convective inertial term and nonlinearity of the system. Typical boundary conditions are no-slip at the wall interface, but nonlinearities may still be introduced through boundary conditions and surface interactions found at small scales. If we were analyzing a nanofluidic channel for instance, the slip boundary condition may need to be taken into account.

13.2.3.4 Dimensionless Parameters

13.2.3.4.1 Particle Reynolds Number

While channel Reynolds number is important when analyzing flow conditions that occur in a microchannel, particle Reynolds number is a crucial dimensionless number when analyzing particle dynamics in the channel. In many of the passive and active separation techniques that will be discussed in the following sections, particle Reynolds number defines the way forces influence motion of particles:

$$Re_p = Re_c \frac{a^2}{{D_h}^2} = \frac{\rho u_f a^2}{\eta D_h} \tag{13.19}$$

Here a is particle radius, ρ is density, u_f is fluid velocity, η is viscosity, and D_h is the hydraulic diameter of the channel. When $Re_p \ll 1$, viscous forces dominate particle motion whereas when $Re_p \gg 1$, inertial forces dominate [30, 31]. The influence of these inertial forces is discussed in Sect. 13.4.

13.2.3.4.2 Blockage Ratio

The size of the particle in relation to the channel dimensions will also play a role in flow/particle interactions [30]:

$$\kappa = \frac{a}{D_h} \tag{13.20}$$

Here a is particle radius and D_h is hydraulic diameter of the channel. This will again have an influence on the migration of particles when both Reynolds numbers are greater than one and inertial forces dominate flow.

13.2.3.4.3 Dean Number

Some microfluidic devices have Reynolds numbers close to or greater than one that cannot be approximated using Stokes flow. This is a result of induced inertial effects caused by certain channel geometries and flow conditions. If a microfluidic device has a curved channel, where the radius of curvature (r) is larger than that of the channel radius (R), fluid with a higher velocity in the center of the channel will be carried to the outer wall due to an induced centrifugal force on the fluid. Fluid at the walls, which is usually stagnant, will now recirculate inward to the middle of the channel causing two symmetric vortices that rotate in opposite directions to form. This secondary flow phenomenon is known as Dean flow. The magnitude of Dean flow can be characterized by the dimensionless Dean number which was first developed by Dean in 1928 [32] and investigated further by Berger et al. in 1983 [33]:

$$De = Re_c \left(\frac{D_h}{2r}\right)^{1/2} \tag{13.21}$$

The Dean number depends on channel Reynolds number (Re_c), hydraulic diameter (D_h), and radius of curvature (r). As the Dean number increases, the vortices will shift their centers closer to the outside wall and a boundary layer will develop. While this secondary force can help to increase mixing at the microscale, it can also be tuned to separate heterogeneous populations of cells. Several examples of this application are discussed in Sect. 13.3.1.3.

13.2.3.4.4 Péclet Number

Since most microfluidic devices have a low Reynolds number and Stokes flow is applied, inertial forces are negligible and mixing is very difficult since diffusion becomes the main method of transport. Mixing in a microfluidic device can require very large time scales, which can be either desired or undesired depending on the application. In the case of devices used for rapid detection of viruses such as HIV, it is imperative that mixing of reagents and samples takes place in a timely manner. The gold standard in detection, known as an ELISA (enzyme-linked immunoassay), requires several mixing and washing steps. Therefore, in order for a microfluidic device to be successful in detecting the virus, it must be capable of replicating some of these steps. On the other hand, for devices whose main objective is to separate rare cells, it is imperative to control mixing. Keeping subpopulations of cells

separate is crucial to the success of the devices. One way to determine the amount of mixing that will occur is to use the ratio of convection to diffusion [34], which is described using the dimensionless Péclet number (*Pe*):

$$Pe = \frac{\text{convection}}{\text{diffusion}} = \frac{Uw}{D} \tag{13.22}$$

where width (w), velocity (U), and the diffusion coefficient (D) comprise the equation. Since the *Pe* number depends on the diffusion coefficient of objects, this alone can be used to separate cells of different sizes and diffusion constants. According to Stokes-Einstein relation, the diffusion coefficient of a particle is inversely proportional to its size

$$D = \frac{kT}{6\pi\eta a} \sim \frac{1}{a} \tag{13.23}$$

where k is Boltzmann's constant, T is temperature, η is dynamic viscosity, and a is the radius of the particle. Therefore, since large objects typically have smaller diffusion coefficients and diffuse slower than small objects, this phenomenon can be used to separate cells of different sizes. In 1996, Brody et al. developed a simple H-filter capable of separating molecules such as solute ions ($a = 0.1$ nm) from viruses (100 nm) and mammalian cells (10 μm) [35]. A small particle such as a solute ion has a high *Pe* number characterized by a large diffusion coefficient and small diameter, whereas a mammalian cell has a large *Pe*. This results in the small particles diffusing to one side of the channel while the larger particles are restricted to the opposite side. The mean square distance (width) the particles will travel in the microchannel can be defined as

$$w = \sqrt{2Dt} \tag{13.24}$$

where w is width, D is the diffusion coefficient of the particle in the media, and t is the time it takes the particle to reach the other side. It is possible to determine the time it takes particles to diffuse a certain distance using this equation:

$$t \sim \frac{w^2}{D} \tag{13.25}$$

13.2.4 Particle Dynamics

Now that we have gone into detail about the fluid dynamics of the system, it is important to look at what is happening to the cells as they are flowing down the length of the channel. We will do so using a force balance analysis on a single cell

in order to determine which forces dominate and how they play a role in separation. For simplification purposes, a cell is assumed to take the shape of a sphere. Realistically, many of the cells we are interested in separating, such as red blood cells (RBCs) and cancer cells, are not spherical in shape and have the ability to deform. In order to generalize the balance of forces for many different cases and to simplify calculations, a sphere will be sufficient [27, 28]. The cell will be considered much smaller than the channel it is traveling in as a way to reduce any local effects that may be induced in the overall flow. This is a realistic scenario since cells typically have diameters of 8–10 μm whereas channel width and height are usually 100 μm. First, we will derive Stokes drag and expand from there.

13.2.4.1 Stokes Drag

If we revisit Stokes laws to describe a particle of radius a moving in a fluid, we can solve for the radial and colatitudinal velocities, in spherical coordinates, analytically as demonstrated by Kirby's "Micro- and Nanoscale Fluid Mechanics" [27].

Radial velocity:

$$u_{\mathrm{r}} = u_{\mathrm{c}} \cos\theta \left(1 - \frac{3}{2}\frac{a}{r} + \frac{1}{2}\frac{a^3}{r^3}\right) \tag{13.26}$$

Colatitudinal velocity:

$$u_{\theta} = -u_{\mathrm{c}} \sin\theta \left(1 - \frac{3a}{4r} - \frac{1}{4}\frac{a^3}{r^3}\right) \tag{13.27}$$

where u_{c} is the velocity of the cell and a is the radius of the cell. Following Kirby [27] we can use these equations to calculate the pressure and viscous shear stress associated with Stokes flow around a sphere.

Pressure:

$$\Delta p = -\eta u_{\mathrm{c}} \frac{3}{2}\frac{a}{r^2} \cos\theta \tag{13.28}$$

Shear stress:

$$\tau = -\frac{3}{2}\frac{a}{r^2} \eta u_{\mathrm{c}} \sin\theta \tag{13.29}$$

These become important when we are attempting to calculate the total force of the fluid on the sphere, which, in this case, is the drag force. In order to do so, we must add all of the surface stresses and integrate over the area of the region. Therefore, we add the normal stress (pressure) and tangential stress (shear stress) together and integrate over the area of the sphere. Doing so results in the Stokes drag equation

where u_c is velocity of the cell, η is dynamic viscosity of the medium, and a is the radius of the cell:

$$F_{\text{drag}} = 6\pi\eta a u_c \tag{13.30}$$

If the cell happens to be rotating in the fluid due to the application of external forces, the drag due to the torque on the cell associated with its angular rotation, ω, is defined as

$$T = 8\pi\eta a^3\omega \tag{13.31}$$

13.2.4.2 Cell in Moving Fluid

Microfluidic devices used to separate rare cell types use continuous flow to their advantage, capitalizing on the balance of forces that occur and manipulating them until separation is achieved. Since we now know Stokes drag, we can use it to determine the force balance on a cell as it is flowing in a microfluidic device, whether the fluid is transporting it alone, as shown in Fig. 13.2, or under the influence of an external force. Since the velocity of the fluid is carrying the cell down the channel, the drag force the cell experiences will increase if cell acceleration increases due to the application of an external force. Mechanical and electrical forces such as inertial lift and dielectrophoresis (DEP) that cause this acceleration to occur are discussed in depth in Sect. 13.4.

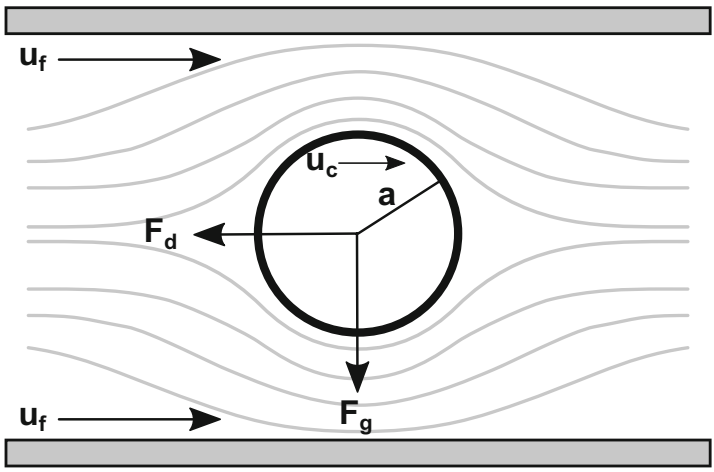

Fig. 13.2 Balance of forces on a cell in viscous flow

For now, we start with deriving the velocity of a cell under the influence of some arbitrary external force using Newton's second law as the foundation shown below:

$$F = m\frac{d\vec{u}_c}{dt} \tag{13.32}$$

Knowing that the cell will experience some drag as it is being carried with the fluid, we need to define a suitable equation to describe the force. We can use the following relation where $\vec{u}_c$ is the velocity of the cell and f is the friction factor which is dependent on the shape of the cell under investigation. Taking into account the fact that the cell will be moving at a different velocity ($\vec{u}_c$) than the fluid ($\vec{u}_f$), our drag force is defined in terms of the relative velocity of the particle:

$$F_d = -f(\vec{u}_c - \vec{u}_f) \tag{13.33}$$

For the sake of simplification, we will assume that the cell is spherical and therefore using Stokes law, we are able to define the friction factor as

$$f = 6\pi\eta a \tag{13.34}$$

where again η is dynamic viscosity. Using these equations, we can expand Newton's second law:

$$F_{ext} - f(\vec{u}_c - \vec{u}_f) = m\frac{d\vec{u}_c}{dt} \tag{13.35}$$

Dividing by mass and rearranging the equation yields a linear, first-order differential equation that can be easily solved by multiplying by an appropriate integrating factor and integrating the equation. This gives us the velocity of the cell in terms of the external force, drag force, and velocity of the fluid:

$$\vec{u}_c = \frac{F_{ext}}{f} + \vec{u}_f\left(1 - e^{-\frac{f}{m}t}\right) \tag{13.36}$$

With the equation above, we can see that the exponential term is due to the acceleration of the cell under the applied external force and the time constant for acceleration is defined as follows:

$$\tau = \frac{m}{f} = \frac{\rho\frac{4}{3}\pi a^3}{6\pi\eta a} = \frac{2\rho a^2}{9\eta} \tag{13.37}$$

For a typical cell, that has a diameter of 10 μm and the same density (ρ) and fluid viscosity (η) as water, we can calculate the time constant for acceleration to be 0.02 μs. Therefore, for times that are much larger than the characteristic time for

acceleration (τ), we can take the limit of the velocity equation as $\tau \to 0$ and find that we are left with the terminal velocity of the cell, which is independent of time:

$$\vec{u}_c = \frac{F_{ext}}{f} + \vec{u}_f \tag{13.38}$$

This means that the cell is no longer accelerating and has reached a constant velocity. From Eq. (13.38), we see that this velocity is a combination of the fluid's velocity and the velocity caused by the external force. Therefore, since the characteristic time constant for acceleration of a cell with a diameter of 10 μm $\left(\tau \sim 10^{-8}\,\mathrm{s}\right)$ is usually much smaller than what can be observed experimentally $(t \sim 0.03\,\mathrm{s})$ [36], the cell can be assumed to have reached its terminal velocity, which may be approximated by Eq. (13.38) in any further modeling.

13.2.4.3 Gravity

The main external force that a cell experiences while suspended in a fluid is gravity. It is possible to perform a force balance on the cell using Stokes' law.

Figure 13.3 shows that gravity is pulling the cell down in the channel causing sedimentation while the drag force is acting upwards against gravity. The force due to gravity is described with the equation below:

$$F_g = V_c(\rho_c - \rho_f)g \tag{13.39}$$

where the volume of the cell is denoted as V_c, g is the gravitational constant, ρ_c is the density of the cell, and ρ_f is the density of the fluid. When gravity is balanced with drag force, the equation becomes

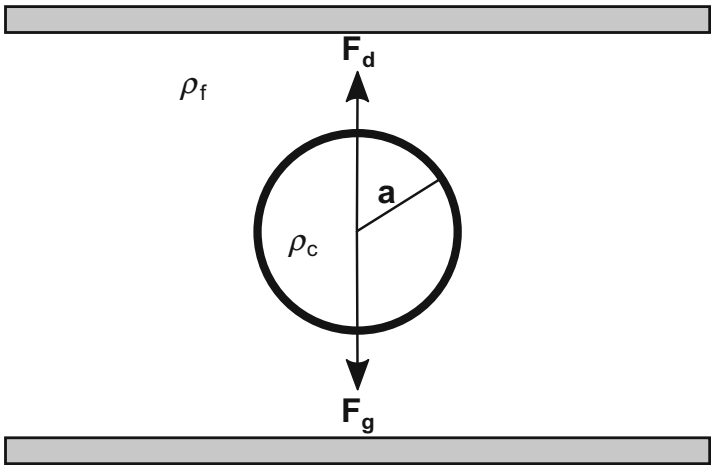

Fig. 13.3 Sedimentation of a cell in viscous flow

$$f^* u_g = V_c(\rho_c - \rho_f)g \tag{13.40}$$

where u_g is the velocity of the cell due to gravity and f is Stokes drag on the cell. Substituting both the equation for volume of a sphere and Stokes drag (Eq. 13.30) results in the final equation for velocity of a cell in a gravitational field:

$$u_g = \frac{2}{9}\frac{a^2(\rho_c - \rho_f)g}{\eta} \tag{13.41}$$

13.2.4.4 Magnus Effect

In the analysis of the above situation, it was assumed that the cell in question was simply translating in the flow and not rotating due to viscous effects. This is an ideal case where Reynolds number is assumed zero and Stokes flow is applied, but this is not always what occurs in actual flow. In microfluidic devices used to separate rare cells, it is possible for these cells to experience rotation $Re \sim 1$ in the fluid flow as shown in Fig. 13.4 [37].

This may drastically affect flow streamlines around the cell and as a result affect the influence that drag force, pressure, and viscous shear stress have on cell motion. During rotation, the no-slip condition still applies and causes the fluid on the surface of the cell to move along with it, where instead of simply translating the fluid also begins to rotate [38, 39]. On the top side of the cell, the fluid follows the rotation of the cell because of the no-slip boundary condition, and begins to flow in the same direction that the cell is rotating. On the bottom side of the cell, fluid continues to flow downstream opposing the rotating flow at the top of the cell. This causes an

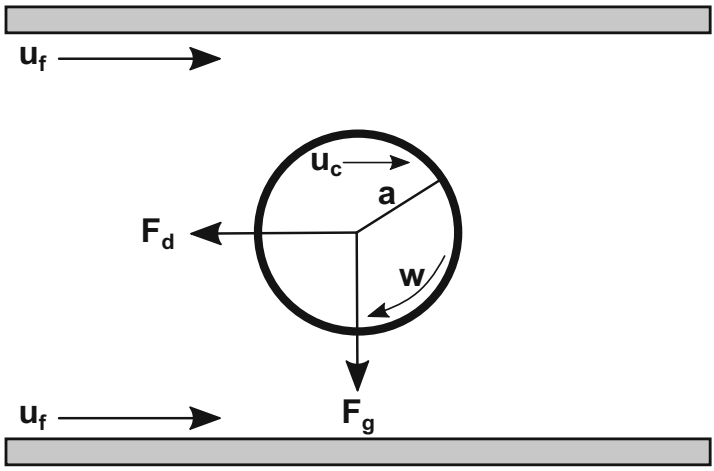

Fig. 13.4 Rotation of a cell in viscous flow

imbalance of pressures at the surface, therefore causing the flow of fluid on the bottom of the cell to stagnate and the flow on top to curve downward along with the cell. Due to Newton's third law, a force equal and opposite is created in a direction normal to the cell's axis of rotation, therefore creating a lift force that pushes the cell upward. This is known as the *Magnus effect* or *Magnus force* [40]:

$$F_{\text{mag}} = 4\pi a^3 \rho_{\text{f}} \left[\vec{\omega} \times (\vec{u}_{\text{c}} - \vec{u}_{\text{f}}) \right] \tag{13.42}$$

where ω is the angular velocity of the cell, ρ_{f} is the density of the fluid and other constants are defined in Sect. 13.2.4.2.

13.2.4.5 Buoyancy Due to Thermal Effects

When applying an electric field to drive flow or separate cells from a heterogeneous population using dielectrophoresis (DEP), thermal gradients may develop because of joule heating in the channel, causing the density of the fluid to change as well. This gradient in density results in a buoyant force on the cell causing lift:

$$F_{\text{b}} = \Delta\rho_{\text{f}} V_{\text{c}} g = \frac{\partial \rho_{\text{f}}}{\partial T} V_{\text{c}} \Delta T g \tag{13.43}$$

where T is temperature and g is the gravitational acceleration on the particle. Buoyancy can usually be neglected in many mechanical separation techniques due to the fact that heating is not generated in the device. In electrical separation techniques, buoyancy is also usually neglected since DEP force dominates the system, therefore minimizing the effect buoyancy has on the cell.

13.3 Mechanical Methods of Rare Cell Isolation

If we revisit the basic force balance on a cell found in Sect. 13.2, we can see that there may be an external force acting on the cell as described in Sect. 13.2.4.2. In terms of rare cell isolation, these forces may be passive or active. Passive forces are inherent in the fluid flow as a consequence of channel geometry or cell behavior, whereas active forces require the application of an external force such as an electric field. Here, we present several examples of passive separation techniques that involve mechanical forces acting on the particle. Specifically, inertia and secondary Dean flow will be discussed.

13.3.1 Inertial Forces

As discussed in Sect. 13.2.3.3, most devices have a Reynolds number much less than one, but in the case of a channel with a width of 100 μm and fluid velocity of 1 cm/s, it is possible to have a Reynolds number of one. If channel dimensions or fluid velocity happen to be larger, the Reynolds number can be greater than one, allowing inertial effects to enter the equation. Inertial effects were first documented and studied by Segré and Silberberg in 1961 [41]. In their investigation of laminar flow in a cylindrical pipe, they found that spherical particles initially in a uniform distribution, position themselves in an annulus ~0.6 times the radius of the pipe. This phenomenon was coined the *tubular pinch* effect and the points where particles migrated became known as the equilibrium positions. This was also studied and characterized for channels with rectangular cross sections and it was found that four equilibrium positions exist and are symmetric along the cross section of the channel [42]. In order to explain this phenomenon, several studies [30, 43–46] determined that this lateral migration of particles occurs due to inertial lift forces acting on the particles in conjunction with Stokes drag. These inertial forces are shown in Fig. 13.5. The wall repulsion force (F_{wL}) is caused by the fact that movement of the particle creates an axisymmetric vorticity wake distribution which is disrupted by the presence of the nearby wall [39]. This induces a velocity, which acts to push the particle away from the wall. The shear gradient lift force (F_{SL}), due to the parabolic velocity profile, acts to push particles away from the centerline.

These forces balance one another at certain locations in the channel, therefore establishing an equilibrium. Channel geometry, particle size, and particle Reynolds number can have a significant effect on how these inertial lift forces influence the motion of the particle. Initially, studies indicated that as long as the blockage

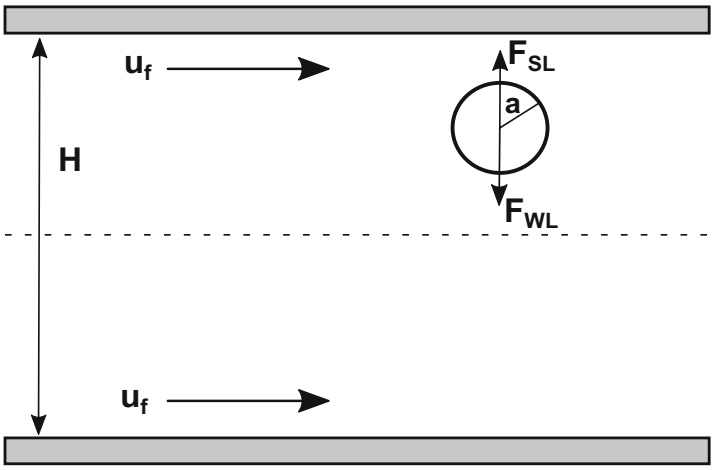

Fig. 13.5 Inertial lift forces on a cell

ratio (κ) and particle Reynolds number (Re_p) were much less than one, the particle will not influence flow conditions and lift force will be uniformly distributed along the channel [30]. The lift force can then be described by $F_L = \left(\rho U_f^2 a^4\right)/H^2$ where ρ is the density of the fluid, U is the velocity of the fluid, a is the radius of the particle, and H is the characteristic length of the channel. Di Carlo et al. [31, 47] further investigated the lift force in confined flows and determined that depending on the aspect ratio of the channel, particle position, and Reynolds number, the lift force can vary. If the blockage ratio approaches one, the lift force may act on the particle differently depending on its position in the channel. Near the wall, it can be described as the following:

$$F_{Lw} = \frac{f_c \rho {U_f}^2 a^6}{H^4} \tag{13.44}$$

whereas at the centerline, it is described by

$$F_{Ls} = \frac{f_c \rho {U_f}^2 a^3}{H} \tag{13.45}$$

where f_c is the dimensionless lift coefficient, which is dependent on distance from the channel wall and channel Reynolds number [48]. A higher channel Reynolds number, Re_c, was found to decrease lift force near the wall ($F_{Lw} \downarrow$) and increase lift force near the centerline ($F_{Ls} \uparrow$). Therefore, as Reynolds number increases, the particles in the channel are pushed toward the walls even more.

Since aspect ratio of the channel, particle size, and the Reynolds number of the channel can influence the lift forces that the particle experience, these parameters can be varied in order to isolate and capture cells of interest [31, 48, 49]. Several devices that apply inertial separation techniques are discussed in the following sections.

13.3.1.1 Straight Microchannels

As aspect ratio (AR) becomes larger $\left(\frac{h}{w} \sim 2\right)$, the number of equilibrium points along the channel cross section will decrease due to the fact that the shear gradient lift force is weakened. In a straight, rectangular cross section, particles will focus at the center of the longer, side channels. Many researchers have taken advantage of this phenomenon and used it to focus and subsequently separate cells of interest. Since inertial lift force scales with particle radius, larger particles will migrate faster than smaller particles to their respective equilibrium positions. Therefore, larger cells will separate from smaller cells and can be collected using bifurcating outlets. Bhagat et al. [50, 51] used this technique to design a microfluidic device capable of continuously filtering 1.9 μm polystyrene beads from a mixture

containing 590 nm polystyrene beads [50, 51]. Hur et al. [52] also successfully filtered adrenal cortical progenitor cells from heterogeneous tissue samples using a similar design.

Recently, Wang et al. [53] focused particles of different sizes into a single stream and were able to perform on-chip flow cytometry at a throughput of 850 cells/s. The device consists of a low AR channel, which causes particles to migrate to equilibrium positions at the center of the top and bottom channel walls. This single channel is then bifurcated into two high AR channels with different hydrodynamic resistances (Fig. 13.6a). This difference in channel resistance causes the flow to separate asymmetrically in accordance with the resistance values and all particles begin to trace the inner wall of channel one. Due to the high AR, after a certain length, the particles no longer form two equilibrium positions, but migrate to a single focal position at the center of the channel. Using numerical and experimental techniques, the optimal resistance ratio (R_1/R_2) between the two bifurcating channels and channel Reynolds number ($Re_c = 40$) were found. A Reynolds number any lower than 40 would have resulted in a decrease of inertial lift forces and any higher would result in more equilibrium positions, therefore lowering efficiency of the device. Efficiency of separation with these optimized parameters was ~99 %. Initially, fluorescent beads 15 μm in diameter were tested, but the device proved to be effective on different sized beads and cells. Microbeads with a $\geq$ 15μm diameter obtained an efficiency >99 %, microbeads with a $\leq$10 μm diameter obtained an efficiency of 55 %, and mouse fibroblasts ($a \sim 17$ μm) obtained an efficiency near 100 %. Incorporating flow cytometry into the device using a laser to count cells downstream led to a relatively high throughput for both beads (2200 beads/s) and fibroblasts (850 cells/s) at a flow rate of 0.15 mL/min. Recovery rate was ~99 % although no post-separation analysis was performed to confirm this. Although throughput for this device is higher than many microfluidic separation techniques, it is still not comparable to gold standards such as fluorescence-activated cell sorting (FACS). Inertial forces can also cause cell lysis, potentially affecting the phenotype and gene expression of cells; yet this was not investigated. Despite the high separation efficiency and relatively high throughput, straight channels operate at a low flow rate and Reynolds number, therefore limiting the amount of cells they can process at one time. The devices also do not offer multiple stages of separation that may lead to a higher outlet purity than is achieved in a single channel. These limitations have been resolved by combining inertial focusing with microscale vortices, which is discussed in the next section.

13.3.1.2 Microscale Vortices

Designing symmetric side reservoirs along a straight, high AR channel induces the formation of vortices and sheath flow (Fig. 13.6b). Due to the sharp expansion of the channel width at each reservoir, the wall-induced lift force becomes small and shear gradient dominates, pushing particles into the vortex. The lift velocity, U_L, scales as the fluid velocity squared multiplied by the particle radius ($U_f^2 a$).

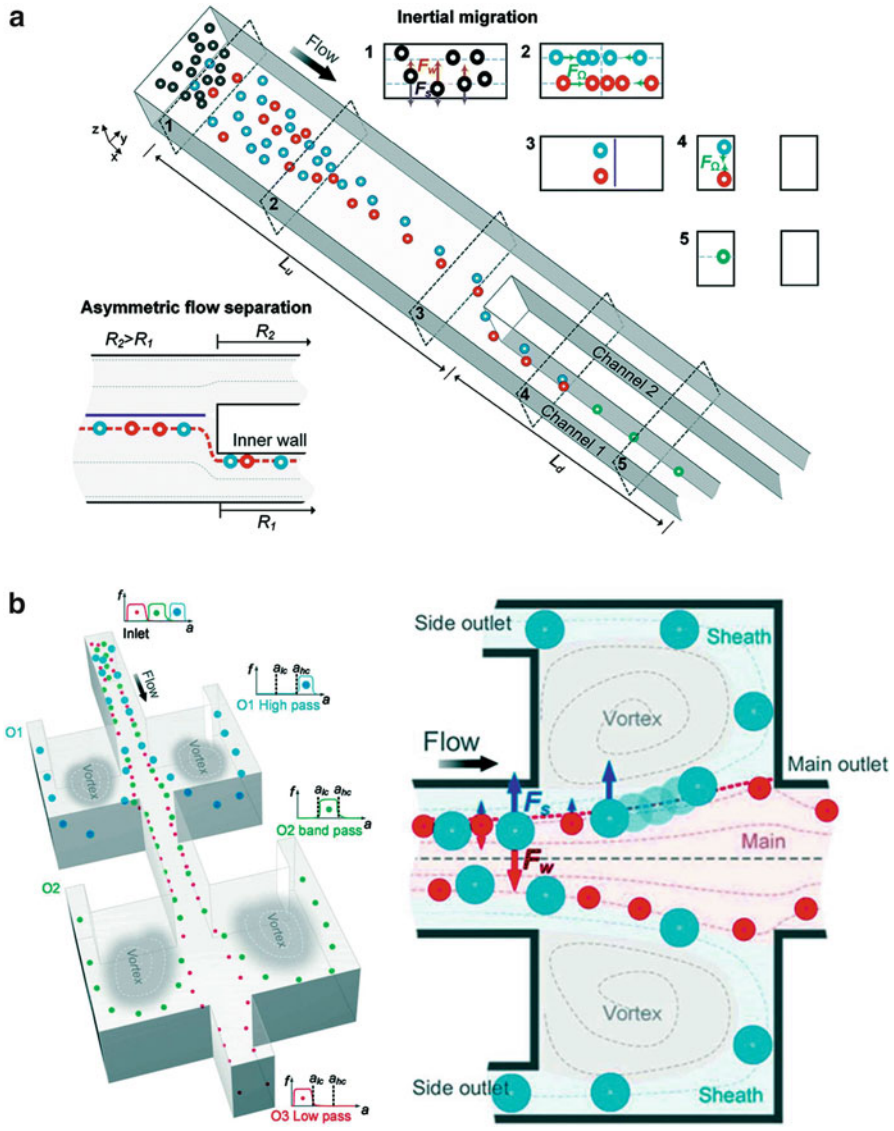

Fig. 13.6 Inertial microfluidic devices for cell separation. (**a**) A single low-aspect-ratio channel is bifurcated into two, high-aspect-ratio channels with different hydrodynamic resistances causing cells to become focused along the inner wall (adapted from Ref. 53 with permission of The Royal Society of Chemistry). (**b**) A continuous, multimodal separation device that uses microscale vortices to trap cells of different sizes (adapted from Ref. 59 with permission of The Royal Society of Chemistry)

Therefore, larger particles migrate across streamlines faster and quickly become entrained in the vortex and sheath flow, while small cells remain in the center channel flow. Several researchers have used this technique to separate polystyrene beads with diameters ranging from 6 to 20 μm [54], cancer cells from blood [55, 56], and pleural effusions [57]. Despite successful separation at a relatively high throughput, these devices had an average efficiency ~60 %, which is much lower than conventional techniques. This may be because the trapping mechanism is not continuous, therefore leading to a threshold number of cells and particles that are allowed to stay entrained in the vortex. If this threshold number is exceeded, cells may circulate out of the vortex and back into the main flow. Moreover, once the entire sample is processed, and the important cells captured, the extraneous cells need to be washed from the main channel before isolated cells are released. During this process, isolated cells may leave the vortex and become washed out with the main flow. As a result, continuous separation methods were developed to minimize this loss of efficiency experienced during the washing step [58].

Recently Wang et al. [59] developed a microfluidic device which uses a two-stage, continuous vortex design to enhance purity, resolution, and efficiency of separation using only one inlet. The device consists of a straight, high AR channel with symmetric reservoirs on each side of the channel (Fig. 13.6b). First, polymer microspheres were used as a proof of concept to test the device at a concentration of 4×10^4per mL. These microspheres ranged in size from 10 to 27 μm. Flow rate and resistance ratio between the side reservoirs and main channel (r/R) were optimized using numerical and experimental techniques. The authors found the optimal resistance ratio and flow rate to be $r/R = 5.4$ and 500 μL/min, corresponding to a channel Reynolds number of 110. This led to a cutoff separation diameter, a_c, for the particles of 14 μm. It was found that the cutoff diameter has a sensitive relationship to both resistance ratio $\left(a_c \sim (r/R)^2\right)$ and fluid velocity ($a_c \sim U_f$). Multimodal cascading is therefore more complicated than it seems because resistance of the channels as well as inlet velocity must be precisely balanced in order to optimize cutoff diameter. The authors investigated how resistance ratios of different branches of the device affect particle separation. The upstream chamber (O1) has a resistance ratio (R_1/R_c) of 4 that is capable of isolating particles with a diameter of 21 μm. The downstream chamber has a resistance ratio (R_3/R_4) of 4.9 and separated particles with a diameter of 11 μm. The second branch (O2) was then able to separate particles in between the two ranges at 18.5 and 15 μm. The two-stage design allows for higher separation efficiency. Not only does it prevent loss of cells during a washing step, but also further refines the heterogeneous sample that is injected into the device. Separation efficiency was found to be >90 % for particles with a size difference of ~3 μm and >70 % for particles with a size difference of 1 μm.

Many of the devices mentioned above that are used to separate cells require long channel lengths in order to see inertial forces have an effect on the cells in the fluid. This is because both designs depend heavily on the resistance ratio of two channels,

which is mainly controlled by their lengths. Therefore, in order to increase throughput and efficiency, it is necessary to connect devices in series or parallel leading to increased channel length and longer processing times.

In order to shorten this length and focus cells more quickly, researchers began to curve their microchannels and capitalize on a secondary flow that resulted, known as Dean flow, which is discussed in the next section.

13.3.1.3 Curved Microchannels

As mentioned briefly in Sect. 13.2.3.4, Dean flow occurs when a microchannel is not straight, but instead has a curved geometry. Due to this curve in the geometry, the flow experiences centrifugal effects causing fluid at the midline of the channel cross section to travel outwards, while stagnant fluid at the top and bottom of the channel travels inward, satisfying conservation of mass [32, 48, 60]. As a result, counter-rotating vortices form in the fluid that act in conjunction with inertial lift forces, changing the equilibrium positions of particles. The two dimensionless numbers that characterize this secondary flow are the Dean number and curvature ratio. In Sect. 13.2.3.4 the Dean number is defined as

$$De = Re_{\mathrm{c}}\left(\frac{D_{\mathrm{h}}}{2r}\right)^{1/2} \tag{13.46}$$

where r is the radius of curvature, D_{h} is the hydraulic diameter and the channel Reynolds number (Re_{c}) and curvature ratio $\left(\delta = \frac{D_{\mathrm{h}}}{2r}\right)$ affect how the secondary flow will influence particle dynamics. Since Dean flow affects inertial forces that the particles experience in the channel, it causes a drag force that is in the same direction of the secondary flow. The Dean drag force can be defined as

$$F_{De} \sim \frac{\rho {U_{\mathrm{f}}}^2 a {D_{\mathrm{h}}}^2}{2r} \tag{13.47}$$

where ρ is the density, u_{f} is the flow velocity, a is the particle radius, D_{h} is the hydraulic diameter, and r is the radius of curvature. Particle position in the channel is dependent upon the balance of inertial and Dean drag forces, which act in superposition. If Dean drag (F_{De}) is comparable to inertial lift (F_{L}), these forces have the ability to reduce the number of equilibrium position channel, therefore ordering particles in the channel. If F_{De} is much larger than F_{L}, particles will simply mix due to the dominant centrifugal motion. On the other hand, if F_{De} is less than F_{L}, only inertial forces will act on the particle. Therefore, in order to determine which forces will affect the fluid and influence particle dynamics, it is important to calculate the ratio of Dean drag and lift forces as defined by Matas et al. and later Di Carlo et al. [48, 61]:

$$\frac{F_{\mathrm{L}}}{F_{De}} \sim \frac{2ra^2}{{D_{\mathrm{h}}}^3} \tag{13.48}$$

Many research groups have capitalized on this phenomena using expansion/contraction designs [62–64] and spiral microchannels [65–70].

Reese et al. [71] recently demonstrated that combining straight and asymmetrically curved microchannels in series provides quicker focusing and higher efficiency. Single- and multi-stage device configurations were tested as a means to increase sample purity and efficiency. The authors tested several device configurations. The first to be tested was a straight, low AR channel with an expansion near the outlet (a), second was a high AR asymmetrically curved channel followed by a straight channel expansion (b), and third was a high AR straight channel followed by a channel expansion (c) (Fig. 13.7a). Polystyrene beads with a diameter of 9.9 μm were injected into the devices at a concentration of 2×10^6 beads per mL and velocity of 0.5 m/s $\left(Re_{\mathrm{p}} = 1.5\right)$. As expected, in devices (a) and (c), particles were focused at their equilibrium positions along the centers of the top and side walls, respectively. At the channel expansion, particles in device (a) became unfocused and occupied 20 % of the channel area. Device (b) performed better with particles occupying about 5 % of the channel and device (c) performed the best with particles only occupying 2 % of the channel area. This is because Dean flow focuses the particles into a single stream that traces the inside wall of the curvature. When particles exit into the expansion, the average fluid velocity decreases, in turn also decreasing interparticle spacing. The fact that the asymmetrically curved channel reduced the number of equilibrium positions to one therefore leads to better focusing in the expansion. Next, a four-stage device was tested to determine if combining more focusing techniques in series would lead to an increase in efficiency. As seen in Fig. 13.7b, a wide straight channel was followed by a wide asymmetrically curved section, a straight high AR section, and finally a channel expansion with three outlets for collection. Section 1 was used to focus particles into two vertical equilibrium positions centered along the channel width. Section 2 caused migration of the particles to one side of the microchannel and section 3 functioned to space the particles and laterally align them before entering the expansion. Outlets 1 and 2 served to collect the concentrated solution while the remaining outlet collected any of the remaining bulk sample. Solutions from outlets 1 and 2 were re-injected into the device and processed three more times. By pass number four, a 25-fold increase in the concentration of particles was reached and a total of $\sim 50 \times 10^6$ beads were collected.

While the device was successful in increasing concentration of particles with each pass through the four stages, separation of different sized particles was not investigated. This is a significant limitation in terms of rare cell isolation, but may serve beneficial in other sample-handling processes such as washing steps that require centrifugation for complete removal of reagents.

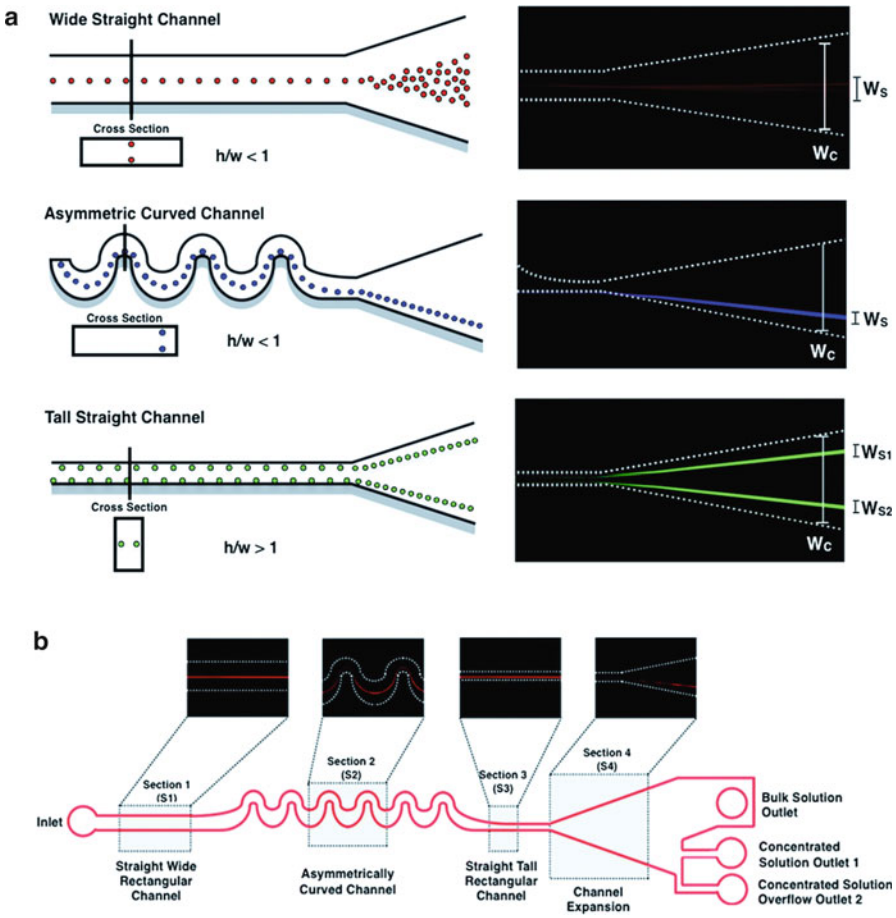

Fig. 13.7 Four-stage curved device for cell focusing. (**a**) Three channel designs used to optimize cell focusing (adapted from Ref. 71 with permission of The Royal Society of Chemistry). (**b**) Schematic of entire device showing the optimized design (adapted from Ref. 71 with permission of The Royal Society of Chemistry)

13.4 Electrical Methods of Rare Cell Isolation

Dielectrophoresis (DEP) is the motion of a particle due to its polarization in a nonuniform electric field. Using this technique, particles can be separated in solution. Different types of cells in particular, but also DNA, and proteins, have been separated via dielectrophoresis based on their intrinsic polarizability [72–75]. The application of microfluidic chips has been useful in, as they have been utilized to design systems with low Reynolds number regimes and high electric field gradients. The high electric field gradients induce a dipole in the cell,

dependent on its properties, and can be used to manipulate the cell through a specific balance of fluidic and electric forces [76]. The DEP force that is exerted on a cell depends on certain properties of that cell in an electric field, and can permit users to sort cells and small particles by features such as malignancy, size, viability, cell type, and other factors [77–81]. The application of microfluidic devices for dielectrophoresis allows this technology to be easily and efficiently transferred into low-cost medical devices [80].

13.4.1 Electrochemical Properties of Cells

The cellular environment has many different properties that can affect the polarizability of a cell, thus leading to a unique electromechanical behavior that can act as that cell's signature. Cellular properties create an intrinsic polarizability of the cell [73]. When the cell is placed under an electric field, free charges align to create a dipole within the cell. Some properties of the cells that can influence this cellular polarizability are amino acid content, interaction between charged areas of amino acids and the water molecules around the cells, structure and rigidity of the lipid bilayer membrane, as well as other factors [73, 82–84]. For more information on the biophysics of cells, please see the review by Pethig and Kell, "The passive electrical properties of biological systems: their significance in physiology, biophysics and biotechnology" [82].

13.4.2 DEP Theory

DEP relies on an important property of cells—their intrinsic polarizability, which allows them to induce an electric dipole in the presence of an electric field. When this dipole is induced within the cell, a force of attraction or repulsion can form between the cell and another cell, or between the cell and objects in the microfluidic channel. These forces induced by dielectrophoresis have been derived in other publications, such as in the review of dielectrophoretic theory by Pethig [73]. The dielectrophoretic force is usually written as

$$\overrightarrow{F_{\mathrm{DEP}}} = 2\pi\varepsilon_{\mathrm{m}} r^3 Re[K(\omega)]\nabla\left(\left|\vec{E}\right|^2\right) \tag{13.49}$$

In this equation, ε_{m} is the permittivity of the medium, r is the radius of the particle of interest, and $K(\omega)$ is the Clausius-Mossotti factor as a function of ω, the angular frequency of the electric field. The root mean square of the electric field is represented by $\vec{E}$. The Clausius-Mossotti factor is a constant throughout the electric field, and is dependent on cell polarizability, medium polarizability, conductivity of the medium, and frequency of the electric field. The gradient of the electric field is

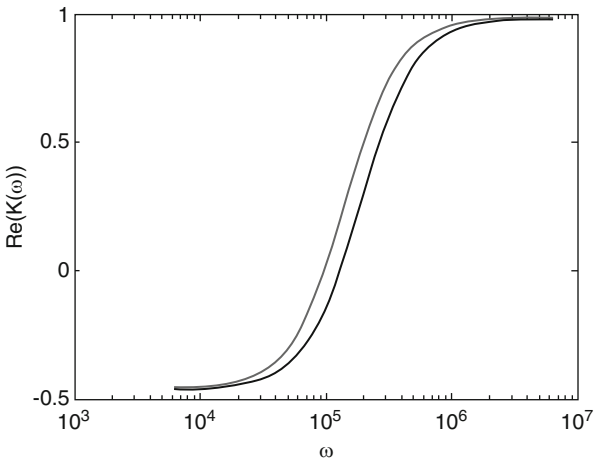

Fig. 13.8 Clausius-Mossotti factor plotted for different frequencies using the single-shell model [70]

spatially dependent, and can be determined computationally for complex geometries. The real part of the Clausius-Mossotti factor reduces to [73]

$$Re[K(\omega)] = Re\left[\frac{\epsilon_c^* - \epsilon_m^*}{\epsilon_c^* + 2\epsilon_m^*}\right] \tag{13.50}$$

In this equation, ϵ_c^* is the complex permittivity of the cell and ϵ_m^* is the complex permittivity of the medium. In both cases, the complex permittivity is described by $\epsilon^* = \epsilon + \frac{\sigma}{i\omega}$, with ω being the angular frequency of the applied electric field, and σ the conductivity of the medium [73].

Cells with different permittivities will have distinct values for Clausius-Mossotti factor, leading to a difference in the force each cell feels within the chip at a given frequency and local field gradient. This difference in forces is what permits separation. In a microfluidic chip with laminar flow, the trapping force can either act to attract or repel a cell or have very little influence on it. If the force on the cell is not great, the cell will not deviate much from its streamline and will continue to flow as if no electric field were applied. In the presence of a dielectric force, the cell may stick to a part of the device or deviate from its normal streamline.

Frequency-dependent curves for the Clausius-Mossotti factor can have a shape such as what is shown in Fig. 13.8. The differences between these curves allow for differences in DEP forces felt by cells and variation of the cell pathway in a device.

13.4.2.1 Negative vs. Positive Dielectrophoresis

Depending on the applied frequency and the electrical properties of the cell and the suspending medium, the DEP force can be either negative or positive. Negative dielectrophoresis (nDEP) is when the cell experiences a repelling force from

regions of higher electric field gradient. The electrodes within the channel push away any cell with the appropriate polarizability given the frequency and voltage of current applied in the channel. Conversely, positive dielectrophoresis (pDEP) is a system in which the cells are attracted to regions with higher field gradients. While negative dielectrophoresis is good for redirecting flow of cells based on their polarizability, positive dielectrophoresis is good for cell trapping. However, cells can be trapped or redirected with either method, depending on the force balance between the drag on the particle and the dielectrophoresis forces.

In a proof of concept, researchers have designed negative dielectrophoresis traps to immobilize cells on a chip [85]. Another group reported using negative dielectrophoretic design to pattern liver cells on a chip, by repelling cells from certain areas of the chip and causing them to land in designated patterns [86]. Using a quadrupole device, another group was able to determine blood type by localizing the crossover frequency (where negative dielectrophoresis switches from positive dielectrophoresis) for a set of blood cells [87].

The magnitude of the dielectric force is a function of the medium permittivity, cell permittivity, magnitude of the applied electric field, and cell radius. The direction of the force exhibited on the cell, however, is a function only of the electric field in the chip and whether positive or negative DEP is being exerted, and thus can be determined independently of cellular properties, creating an effective field of possible cell-chip interactions. An effective magnitude of force can be developed by normalizing the cell-specific properties, such as the Clausius-Mossotti factor, to the cell-dependent properties. While the magnitude of the force depends on the properties of each individual cell type, the relative magnitude of force in one region vs. another is independent of cellular properties. This effective field of DEP forces is useful in determining chip design and predicting trapping regions. The effective field is

$$\vec{\Gamma} = \nabla\left(\vec{E} \cdot \vec{E}\right) \tag{13.51}$$

For a derivation of this field, please see the paper by Sano et al. *Multilayer contactless dielectrophoresis: theoretical considerations* [88].

13.4.2.2 Multi-Shell Model and Single-Shell Model for Measuring Cell Permittivity

For theoretical calculations of cell polarizability, the cell can be approximated as a set of concentric spherical shells as is shown in Fig. 13.9. These shells define the properties of each layer of the cell and the topology of the related regions. For a typical cell, one could estimate the outer membrane as one shell, the cytoplasm as another, and the nucleus/nuclear envelope as a third. By reducing shells of similar properties into effective shells, it is possible to condense the complex dielectric factor describing the set of concentric rings into its simplified form. Usually the cell

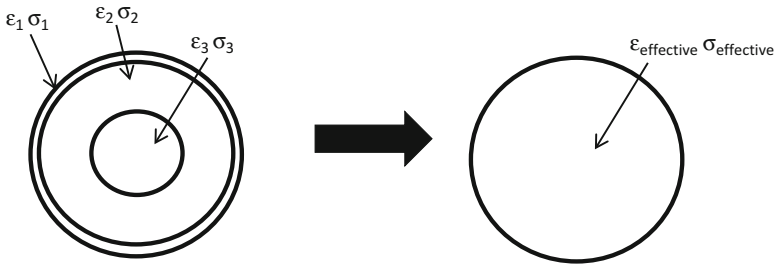

Fig. 13.9 Depiction of the multi-shell model

can be condensed to a single-shell model, taking an effective permittivity inside of the cell. For more information, see Pethig's review, *Dielectrophoresis: An assessment of its potential to aid the research and practice of drug discovery and delivery* [72].

13.4.2.3 Derivation of DEP Force

The DEP force is derived from the intrinsic polarizability of a cell, which can lead to an induced dipole when it flows through a chip. To derive this DEP force from the properties of a cell, we will first start with a dipole in an electric field as is shown in Fig. 13.10. For more detail and mathematical guidance, please see Chap. 2 of *Electromechanics of Particles* by Jones, Cambridge University Press [89].

The cell is not a perfect dipole, but the induced cellular dipole that forms in the presence of the electric field can be estimated as a dipole with a small distance between the two poles $\vec{d}$. Because the electric field is nonuniform in the chip, due to the presence of obstacles and other cells, we must consider the electric field at each point independently, rather than making an assumption about the form of the field. The force on a dipole is then

$$\vec{F} = q\vec{E}\left(\vec{r} + \vec{d}\right) - q\vec{E}(\vec{r}) \tag{13.52}$$

We will assume that we are measuring from a point $\vec{r}$, far away from the dipole. This allows us to say that the distance between the two points in the dipole, $\vec{d}$, is very small in comparison to the distance from which we are measuring. This assumption should be considered valid in a dielectrophoretic chip, as the internal cellular dipole is smaller than the relation between that dipole and other features of the chip. This assumption is made in order to simplify the nonuniform electric field. Otherwise, the electric field would need to be considered separately at $\vec{r}$ and $\vec{d} + \vec{r}$. We can make a Taylor expansion for $\vec{E}\left(\vec{r} + \vec{d}\right)$. This becomes

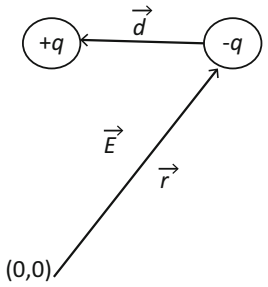

Fig. 13.10 Dipole in an electric field, analogous to a cell in an electric field

$$\vec{E}\left(\vec{r}+\vec{d}\right) = \vec{E}(\vec{r}) + \vec{d}\nabla\vec{E}(\vec{r}) + \cdots \tag{13.53}$$

Because we assumed that $\vec{d} \ll \vec{r}$, we can neglect higher terms than $\nabla E(r)$ as they will be very small. The force on the dipole then can be approximated as

$$\overrightarrow{F_{\text{DEP}}} \simeq q\ \vec{E}\left(\vec{r}+\vec{d}\right) - q\vec{E}(\vec{r}) = q\vec{d}\nabla\vec{E}(\vec{r}) \tag{13.54}$$

This is known as the dielectrophoretic approximation. By definition, the dipole moment, $\vec{p}$, is $\vec{p} = q\vec{d}$. Therefore,

$$\overrightarrow{F_{\text{DEP}}} = \vec{p}\nabla\vec{E}(\vec{r}) \tag{13.55}$$

gives the dielectrophoretic force in a chip [89].

13.4.2.4 Derivation of the Clausius-Mossotti Factor

This derivation also comes from *Electromechanics of Particles* by Jones [89]. Please refer to the book for further information. For a small dipole, the potential of the dipole is given by Φ:

$$\Phi = \frac{q}{4\pi\epsilon_1 r_+} - \frac{q}{4\pi\epsilon_1 r_-} = \frac{q}{4\pi\epsilon_1}\left(\frac{1}{r_+} - \frac{1}{r_-}\right) \tag{13.56}$$

This considers that the point charges are separated by a distance $2r$. In this case, the permittivity constant, ϵ_1, is the permittivity of the medium, as we are considering these point charges to be in the medium of the device. See *Electromechanics of Particles* for more details. This equation for electric potential can be rewritten as a Maclaurin expansion:

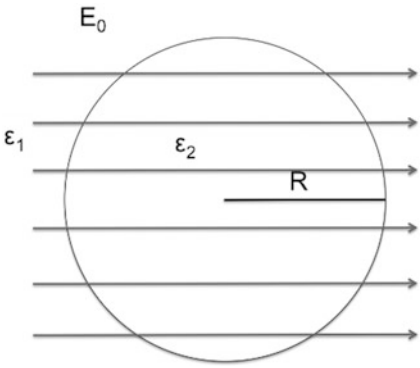

Fig. 13.11 Insulating sphere in uniform electric field

$$\Phi = \frac{qdP_1(\cos\theta)}{4\pi\epsilon_1 r^2} + \cdots \tag{13.57}$$

In this expansion, $P_1(\cos\theta)$ is the first-order Legendre polynomial, which is $P_1(\cos\theta) = \cos\theta$. Taking the first term of the Maclaurin expansion gives the first-order approximation for the potential between two point charges (in this case, the cellular dipole):

$$\Phi \simeq \frac{qd\ \cos\theta}{4\pi\epsilon_1 r^2} \tag{13.58}$$

As before, we know the dipole moment to be $p = qd$, which gives

$$\Phi \simeq \frac{p\cos\theta}{4\pi\epsilon_1 r^2} \tag{13.59}$$

Again, here ϵ_1 would be the permittivity of the medium around the two point charges. We will keep this equation until a bit later. Now, we consider an insulating sphere of radius R in a uniform electric field as is shown in Fig. 13.11. Assuming a first order approximation, this can also be used to describe a lossless particle in a medium, as the cell is not particularly conductive. Because the cell is much smaller than the chip, we make the assumption that the electric field will be mostly uniform when passing through the cell. The permittivity of the medium is taken to be ϵ_1, and the permittivity of the cytoplasm is ϵ_2.

Using Gauss's law, we find the potential inside and outside the sphere. This gives

$$\Phi_1 = -E_0 r\cos\theta + \frac{A\cos\theta}{r^2} \quad \text{outside the sphere} \tag{13.60}$$

$$\Phi_2 = -Br\cos\theta \quad \text{inside the sphere} \tag{13.61}$$

The electric field is continuous at the boundary. The norm of the displacement flux is also continuous at the boundary. Therefore, we must consider the boundary conditions (at $r = R$) to be

$$\Phi_1 = \Phi_2 \tag{13.62}$$

$$-\epsilon_1 \frac{\partial \Phi_1}{\partial r}\bigg|_R = -\epsilon_2 \frac{\partial \Phi_2}{\partial r}\bigg|_R \tag{13.63}$$

Solving for these two equations given the boundary conditions leaves us with a system of equations that can be solved to get A and B. In this case, we find

$$A = R^3(E_0 - B) = R^3 E_0 \frac{\epsilon_2 - \epsilon_1}{\epsilon_2 + 2\epsilon_1} \tag{13.64}$$

$$B = \frac{3\epsilon_1 E_0}{\epsilon_2 + 2\epsilon_1} \tag{13.65}$$

If we plug these back into the equations for Φ_1, Φ_2, we get

$$\Phi_1 = -E_0 r\cos\theta + \frac{R^3}{r^2} E_0 \frac{\epsilon_2 - \epsilon_1}{\epsilon_2 + 2\epsilon_1}\cos\theta \text{ outside the sphere} \tag{13.66}$$

$$\Phi_2 = \frac{-3\epsilon_1}{\epsilon_2 + 2\epsilon_1} E_0 r\cos\theta \text{ inside the sphere} \tag{13.67}$$

Outside the sphere, we have Φ_1, but we also have the equation for two point charges that we derived earlier, $\Phi \simeq \frac{p\cos\theta}{4\pi\epsilon_1 r^2}$. We can set the $1/r^2$ terms equal to each other, as the linear term is referring to the uniform electric field rather than the induced dipole. Doing so, we have

$$\frac{p\cos\theta}{4\pi\epsilon_1 r^2} = \frac{R^3}{r^2} E_0 \frac{\epsilon_2 - \epsilon_1}{\epsilon_2 + 2\epsilon_1}\cos\theta \tag{13.68}$$

We know that for a homogeneous dielectric sphere, $p = 4\pi\epsilon_1 K R^3 E_0$ (see *Electromechanics of Particles*, Chap. 2 for details) [84]. Plugging this in gives

$$K = \frac{\epsilon_2 - \epsilon_1}{\epsilon_2 + 2\epsilon_1} \tag{13.69}$$

This K is the Clausius-Mossotti factor for a lossless dielectric sphere in a medium.

13.4.3 Design of Cell Separation Devices

There have been many studies to show the use of dielectrophoresis to separate cells in microfluidic channels. Remembering the DEP force, $\overrightarrow{F_{\text{DEP}}} = 2\pi\varepsilon_{\text{m}} r^3 Re[K(\omega)]\nabla\left(|\vec{E}|^2\right)$, we see that in order to have any force between the cell

and an object in the channel it is necessary to have a gradient of the electric field. Cell separation can be done based on differences in cell radius and differences in Clausius-Mossotti factor between cells. The Clausius-Mossotti factor, $K(\omega) = \frac{\epsilon_c^* - \epsilon_m^*}{\epsilon_c^* + 2\epsilon_m^*}$, with $\epsilon^* = \epsilon + \sigma/i\omega$, is dependent on the permittivity of the medium, conductivity of the medium, and angular frequency of the electric field, which is the same for all cells in a device, and the permittivity of the cell, which can vary from one cell type to another. For this reason, factors such as the strength of the electric field, frequency of applied voltage, permittivity of the medium, and conductivity of the medium can all be modified to amplify the ratio of forces between two types of cells in suspension. However, as can be seen in Fig. 13.8, whether or not these two particles can be separated is dependent on the permittivity, conductivity, and radius of each cell type as well as the sensitivity of the device design.

Normally, a channel containing a design of electrodes and objects is fabricated, and cells are streamed through the channel at a constant rate. Objects in the channels create inhomogeneities in the electric field, which provide regions that can interact with the cells and elicit a force that will cause them to move according to their dielectric properties. Several of these types of dielectrophoretic mechanisms are discussed here, including contactless dielectrophoresis, insulator-based dielectrophoresis, and variations on these. Many different methods have been used to harness the polarizability of cells and other small molecules for separation, and this list is a small set of what has been done in this field.

13.4.3.1 Classical vs. Insulator-based Dielectrophoresis

Another method of defining dielectrophoresis is by contactless dielectrophoresis (cDEP). Classical dielectrophoresis requires an interdigitated electrode array to be in direct contact with the medium where the cells are, in order to affect the electric field and create a gradient/inhomogeneity for the dielectrophoresis force to be felt. In contrast, insulator-based dielectrophoresis (iDEP) uses insulating structures within the chip to create inhomogeneities in the electric field needed to drive DEP. iDEP has been widely used in a number of applications for cell separation. In addition, the technique has been employed as a method of trapping protein as well as DNA [90], as well as a method of separating membrane protein nanocrystals from solution [79].

13.4.3.2 Contactless Dielectrophoresis

As opposed to classical DEP or iDEP, contactless dielectrophoresis (cDEP) uses an insulating membrane to separate the cells/sample from the electrodes and deleterious electrochemical effects. Similar to iDEP, it utilizes inert insulating structures within the chip to create inhomogeneities in the electric field. This method improves cell viability by preventing direct contact with high-voltage sources [77, 88].

13.5 Conclusion

This chapter outlined the theory and practical implementation of methods of rare cell isolation using microfluidic and bioelectrical methodologies. The ability to capture and isolate rare cells is an important step in the process of being able to diagnose and treat cancer based on the presence of circulating tumor cells and other rare cells of interest to provide early and personalized diagnosis. The development of microfluidics and bioelectrical mechanics in recent years has provided a novel toolbox that can be utilized to improve our ability to obtain study and utilize these cells to improve patient outcomes.

References

1. Tjensvoll K, Nordgård O, Smaaland R (2014) Circulating tumor cells in pancreatic cancer patients: methods of detection and clinical implications. Int J Cancer 134:1–8. doi:10.1002/ijc.28134
2. Alix-Panabieres C, Pantel K (2014) Challenges in circulating tumour cell research. Nat Rev Cancer 14:623–631
3. Nagrath S, Sequist LV, Maheswaran S et al (2007) Isolation of rare circulating tumour cells in cancer patients by microchip technology. Nature 450:1235–1239. doi:10.1038/nature06385
4. Stott SL, Hsu C, Tsukrov DI et al (2010) Isolation of circulating tumor cells using a microvortex-generating herringbone-chip. Proc Natl Acad Sci U S A 107:18392–18397. doi:10.1073/pnas.1012539107
5. Wlodkowic D, Cooper JM (2010) Tumors on chips: oncology meets microfluidics. Curr Opin Chem Biol 14:556–567. doi:10.1016/j.cbpa.2010.08.016
6. Shelby JP, White J, Ganesan K et al (2003) A microfluidic model for single-cell capillary obstruction by Plasmodium falciparum-infected erythrocytes. Proc Natl Acad Sci U S A 100:14618–14622. doi:10.1073/pnas.2433968100
7. Gascoyne P, Satayavivad J, Ruchirawat M (2004) Microfluidic approaches to malaria detection. Acta Trop 89:357–369. doi:10.1016/j.actatropica.2003.11.009
8. Hou HW, Bhagat AAS, Chong AGL et al (2010) Deformability based cell margination—a simple microfluidic design for malaria-infected erythrocyte separation. Lab Chip 10:2605–2613. doi:10.1039/c003873c
9. Cheng X, Irimia D, Dixon M et al (2007) A microfluidic device for practical label-free CD4(+) T cell counting of HIV-infected subjects. Lab Chip 7:170–178. doi:10.1039/b612966h
10. Lee WG, Kim Y, Geun B et al (2010) Nano/microfluidics for diagnosis of infectious diseases in developing countries. Adv Drug Deliv Rev 62:449–457. doi:10.1016/j.addr.2009.11.016
11. Yang BD, Niu X, Liu Y et al (2008) Electrospun nanofibrous membranes: a novel solid substrate for microfluidic immunoassays for HIV. Adv Mater 20:4770–4775. doi:10.1002/adma.200801302
12. Baker CA, Duong CT, Grimley A, Roper MG (2009) Recent advances in microfluidic detection systems. Bioanalysis 1:967–975. doi:10.4155/bio.09.86
13. Chin CD, Laksanasopin T, Cheung YK et al (2011) Microfluidics-based diagnostics of infectious diseases in the developing world. Nat Med 17:1015–1019. doi:10.1038/nm.2408
14. Yager P, Domingo GJ, Gerdes J (2008) Point-of-care diagnostics for global health. Annu Rev Biomed Eng 10:107–144. doi:10.1146/annurev.bioeng.10.061807.160524
15. Chung TD, Kim HC (2007) Recent advances in miniaturized microfluidic flow cytometry for clinical use. Electrophoresis 28:4511–4520. doi:10.1002/elps.200700620

16. Dimov IK, Basabe-Desmonts L, Garcia-Cordero JL et al (2011) Stand-alone self-powered integrated microfluidic blood analysis system (SIMBAS). Lab Chip 11:845–850. doi:10.1039/c0lc00403k
17. Gad-el-Hak M (2001) Flow physics. MEMS Handb. doi:10.1201/9781420050905.ch4
18. Bruus H (2008) Theoretical microfluidics. Physics (College Park Md) 18:363. doi:10.1111/j.1574-6968.2009.01808.x
19. Lei H, Fedosov DA, Caswell B, Karniadakis GE (2013) Blood flow in small tubes: quantifying the transition to the non-continuum regime. J Fluid Mech 722:214–239. doi:10.1017/jfm.2013.91
20. Ali Beskok GEK (1999) report: a model for flows in channels, pipes, and ducts at micro and nano scales. Microscale Thermophys Eng 3:43–77. doi:10.1080/108939599199864
21. Thompson P, Troian SM (1997) A general boundary condition for liquid flow at solid surfaces. Nature 389:360–362. doi:10.1038/38686
22. Ghosh A (2011) Mechanics over micro and nano scales. In: Chakraborty S (ed). Springer, New York, pp 61–94
23. Pianka ER, Vitt LJ (2003) Lizards: windows to the evolution of diversity. University of California Press, Berkeley, CA
24. Trimmer W, Stroud R (2001) Scaling of micromechanical devices. MEMS Handb. doi:10.1201/9781420050905.ch2
25. Munson B, Young D, Okiishi T, Huebsch W (2009) Fundamentals of fluid mechanics, 6th edn. John Wiley & Sons Inc., New York
26. Sia SK, Whitesides GM (2003) Microfluidic devices fabricated in poly(dimethylsiloxane) for biological studies. Electrophoresis 24:3563–3576. doi:10.1002/elps.200305584
27. Kirby B (2010) Micro- and nanoscale fluid mechanics. Cambridge University Press, New York
28. Panton RL (2013) Flow at low Reynolds numbers. In: Incompressible flow. Wiley, New York, pp 607–649
29. Squires TM, Quake SRSR (2005) Microfluidics: fluid physics at the nanoliter scale. Rev Mod Phys 77:977–1026
30. Asmolov ES (1999) The inertial lift on a spherical particle in a plane Poiseuille flow at large channel Reynolds number. J Fluid Mech 381:63–87. doi:10.1017/S0022112098003474
31. Di Carlo D (2009) Inertial microfluidics. Lab Chip 9:3038–3046. doi:10.1039/b912547g
32. Dean WR (1928) Fluid motion in a curved channel. Proc R Soc A Math Phys Eng Sci 121:402–420. doi:10.1098/rspa.1928.0205
33. Berger SA, Talbot L, Yao LS (1983) Flow in curved pipes. Annu Rev Fluid Mech 15:461–512. doi:10.1146/annurev.fl.15.010183.002333
34. Bergman TL, Lavine AS, Incropera FP, Dewitt DP (2011) Fundamentals of heat and mass transfer, 7th edn. John Wiley & Sons, Inc., New York
35. Brody JP, Yager P (1997) Diffusion-based extraction in a microfabricated device. Sensors Actuators A Phys 58:13–18. doi:10.1016/S0924-4247(97)80219-1
36. Morgan H, Green NG (2003) Fluid dynamics. In: Pethig R (ed) AC electrokinetics: colloids nanoparticles. Institute of Physics Publishing, UK, pp 65–80
37. Lei U, Yang CY, Wu KC (2006) Viscous torque on a sphere under arbitrary rotation. Appl Phys Lett 89:20–23. doi:10.1063/1.2372704
38. Panton RL (2013) Ideal Flows in a plane. In: Incompressible flow. Wiley, New York, pp 438–501
39. Zeng L, Balachandar S, Fischer P (2005) Wall-induced forces on a rigid sphere at finite Reynolds number. J Fluid Mech 536:1–25. doi:10.1017/S0022112005004738
40. Rubinow SI, Keller JB (1961) The transverse force on a spinning sphere moving in a viscous fluid. J Fluid Mech 11:447. doi:10.1017/S0022112061000640
41. Segré G, Silberberg A (1961) Radial particle displacements in Poiseuille flow of suspensions. Nature 189:209–210. doi:10.1038/189209a0
42. Chun B, Ladd AJC (2006) Inertial migration of neutrally buoyant particles in a square duct: an investigation of multiple equilibrium positions. Phys Fluids 18:3–6. doi:10.1063/1.2176587

43. Ho BP, Leal LG (1976) Migration of rigid spheres in a two-dimensional unidirectional shear flow of a second-order fluid. J Fluid Mech 76:783. doi:10.1017/S002211207600089X
44. Cox RG, Brenner H (1968) The lateral migration of solid particles in Poiseuille flow—I: Theory. Chem Eng Sci 23:147–173. doi:10.1016/0301-9322(77)90001-5
45. Matas J-P, Morris JF, Guazzelli É (2004) Inertial migration of rigid spherical particles in Poiseuille flow. J Fluid Mech 515:171–195. doi:10.1017/S0022112004000254
46. Schonberg JA, Hinch EJ (1989) Inertial migration of a sphere in Poiseuille flow. J Fluid Mech 203:517–524
47. Di Carlo D, Edd JF, Humphry KJ et al (2009) Particle segregation and dynamics in confined flows. Phys Rev Lett 102:1–4. doi:10.1103/PhysRevLett.102.094503
48. Di Carlo D, Irimia D, Tompkins RG, Toner M (2007) Continuous inertial focusing, ordering, and separation of particles in microchannels. Proc Natl Acad Sci U S A 104:18892–18897. doi:10.1073/pnas.0704958104
49. Zhou J, Giridhar PV, Kasper S, Papautsky I (2013) Modulation of aspect ratio for complete separation in an inertial microfluidic channel. Lab Chip 13:1919–1929. doi:10.1039/c3lc50101a
50. Bhagat AAS, Kuntaegowdanahalli SS, Papautsky I (2008) Enhanced particle filtration in straight microchannels using shear-modulated inertial migration. Phys Fluids 20:101702. doi:10.1063/1.2998844
51. Bhagat AAS, Kuntaegowdanahalli SS, Papautsky I (2009) Inertial microfluidics for continuous particle filtration and extraction. Microfluid Nanofluid 7:217–226. doi:10.1007/s10404-008-0377-2
52. Hur SC, Brinckerhoff TZ, Walthers CM et al (2012) Label-free enrichment of adrenal cortical progenitor cells using inertial microfluidics. PLoS One 7:e46550. doi:10.1371/journal.pone.0046550
53. Wang X, Zandi M, Ho C-C et al (2015) Single stream inertial focusing in a straight microchannel. Lab Chip 15:1812–1821. doi:10.1039/C4LC01462F
54. Zhou J, Kasper S, Papautsky I (2013) Enhanced size-dependent trapping of particles using microvortices. Microfluid Nanofluid 15:611–623. doi:10.1007/s10404-013-1176-y
55. Hur SC, Mach AJ, Di Carlo D (2011) High-throughput size-based rare cell enrichment using microscale vortices. Biomicrofluidics 5:1–10. doi:10.1063/1.3576780
56. Sollier E, Go DE, Che J et al (2014) Size-selective collection of circulating tumor cells using Vortex technology. Lab Chip 14:63–77. doi:10.1039/c3lc50689d
57. Che J, Mach AJ, Go DE et al (2013) Microfluidic purification and concentration of malignant pleural effusions for improved molecular and cytomorphological diagnostics. PLoS One 8:e78194. doi:10.1371/journal.pone.0078194
58. Wang X, Zhou J, Papautsky I (2013) Vortex-aided inertial microfluidic device for continuous particle separation with high size-selectivity, efficiency, and purity. Biomicrofluidics 7:22–25. doi:10.1063/1.4818906
59. Wang X, Papautsky I (2015) Size-based microfluidic multimodal microparticle sorter. Lab Chip 15:1350–1359. doi:10.1039/c4lc00803k
60. Gossett DR, Di Carlo D (2009) Particle focusing mechanisms in curving confined flows. Anal Chem 81:8459–8465. doi:10.1021/ac901306y
61. Matas JP, Morris JF, Guazzelli E (2004) Lateral forces on a sphere. Oil Gas Sci Technol Rev IFP 59:59–70
62. Lee MG, Shin JH, Bae CY et al (2013) Label-free cancer cell separation from human whole blood using inertial micro fluidics at low shear stress. Anal Chem 85(13):6213–6218
63. Lee MG, Choi S, Park J-K (2009) Three-dimensional hydrodynamic focusing with a single sheath flow in a single-layer microfluidic device. Lab Chip 9:3155–3160. doi:10.1039/b910712f
64. Zhang J, Li M, Li WH, Alici G (2013) Inertial focusing in a straight channel with asymmetrical expansion–contraction cavity arrays using two secondary flows. J Micromech Microeng 23:085023. doi:10.1088/0960-1317/23/8/085023
65. Hou HW, Warkiani ME, Khoo BL et al (2013) Isolation and retrieval of circulating tumor cells using centrifugal forces. Sci Rep 3:1259. doi:10.1038/srep01259

66. Nivedita N, Papautsky I (2013) Continuous separation of blood cells in spiral microfluidic devices. Biomicrofluidics 7:1–14. doi:10.1063/1.4819275
67. Sun J, Liu C, Li M et al (2013) Size-based hydrodynamic rare tumor cell separation in curved microfluidic channels. Biomicrofluidics 7:1–11. doi:10.1063/1.4774311
68. Xiang N, Yi H, Chen K et al (2013) High-throughput inertial particle focusing in a curved microchannel: insights into the flow-rate regulation mechanism and process model. Biomicrofluidics 7:1–10. doi:10.1063/1.4818445
69. Tallapragada P, Hasabnis N, Katuri K et al (2015) Scale invariant hydrodynamic focusing and sorting of inertial particles by size in spiral micro channels. J Micromech Microeng 25:084013. doi:10.1088/0960-1317/25/8/084013
70. Xiang N, Chen K, Dai Q et al (2015) Inertia-induced focusing dynamics of microparticles throughout a curved microfluidic channel. Microfluid Nanofluid 18:29–39. doi:10.1007/s10404-014-1395-x
71. Reece AE, Kaastrup K, Sikes HD, Oakey J (2015) Staged inertial microfluidic focusing for complex fluid enrichment. RSC Adv 5:53857–53864. doi:10.1039/C5RA10634F
72. Pethig R (2013) Dielectrophoresis: an assessment of its potential to aid the research and practice of drug discovery and delivery. Adv Drug Deliv Rev 65:1589–1599. doi:10.1016/j.addr.2013.09.003
73. Pethig R (2010) Review article-dielectrophoresis: status of the theory, technology, and applications. Biomicrofluidics 4:1–35. doi:10.1063/1.3456626
74. Martinez-Duarte R, Camacho-Alanis F, Renaud P, Ros A (2013) Dielectrophoresis of lambda-DNA using 3D carbon electrodes. Electrophoresis 34:1113–1122. doi:10.1002/elps.201200447
75. Moncada-Hernandez H, Nagler E, Minerick AR (2014) Theoretical and experimental examination of particle-particle interaction effects on induced dipole moments and dielectrophoretic responses of multiple particle chains. Electrophoresis 35:1803–1813. doi:10.1002/elps.201300636
76. Gascoyne PRC, Vykoukal J (2002) Particle separation by dielectrophoresis. Electrophoresis 23:1973–1983. doi:10.1002/1522-2683(200207)23:13<1973::AID-ELPS1973>3.0.CO;2-1
77. Salmanzadeh A, Romero L, Shafiee H et al (2012) Isolation of prostate tumor initiating cells (TICs) through their dielectrophoretic signature. Lab Chip 12:182–189. doi:10.1039/c1lc20701f
78. Wang X, Becker FF, Gascoyne PRC (2002) Membrane dielectric changes indicate induced apoptosis in HL-60 cells more sensitively than surface phosphatidylserine expression or DNA fragmentation. Biochim Biophys Acta 1564:412–420
79. Abdallah BG, Chao T-C, Kupitz C et al (2013) Dielectrophoretic sorting of membrane protein nanocrystals. ACS Nano 7:9129–9137. doi:10.1021/nn403760q
80. Jones PV, Staton SJR, Hayes MA (2011) Blood cell capture in a sawtooth dielectrophoretic microchannel. Anal Bioanal Chem 401:2103–2111. doi:10.1007/s00216-011-5284-9
81. Shafiee H, Sano MB, Henslee EA et al (2010) Selective isolation of live/dead cells using contactless dielectrophoresis (cDEP). Lab Chip 10:438–445. doi:10.1039/b920590j
82. Pethig R, Kell DB (1987) The passive electrical properties of biological systems: their significance in physiology, biophysics and biotechnology. Phys Med Biol 32:933–970. doi:10.1088/0031-9155/32/8/001
83. Cemažar J, Kotnik T (2012) Dielectrophoretic field-flow fractionation of electroporated cells. Electrophoresis 33:2867–2874. doi:10.1002/elps.201200265
84. Chan KL, Gascoyne PR, Becker FF, Pethig R (1997) Electrorotation of liposomes: verification of dielectric multi-shell model for cells. Biochim Biophys Acta 1349:182–196
85. Nejad HR, Chowdhury OZ, Buat MD, Hoorfar M (2013) Characterization of the geometry of negative dielectrophoresis traps for particle immobilization in digital microfluidic platforms. Lab Chip 13:1823–1830. doi:10.1039/c3lc41292j

86. Puttaswamy SV, Sivashankar S, Chen R-J et al (2010) Enhanced cell viability and cell adhesion using low conductivity medium for negative dielectrophoretic cell patterning. Biotechnol J 5:1005–1015. doi:10.1002/biot.201000194
87. Leonard KM, Minerick AR (2011) Explorations of ABO-Rh antigen expressions on erythrocyte dielectrophoresis: changes in cross-over frequency. Electrophoresis 32:2512–2522. doi:10.1002/elps.201100077
88. Sano MB, Salmanzadeh A, Davalos RV (2012) Multilayer contactless dielectrophoresis: theoretical considerations. Electrophoresis 33:1938–1946. doi:10.1002/elps.201100677
89. Jones TB (1995) Electromechanics of particles. Cambridge University Press, Cambridge
90. Camacho-Alanis F, Gan L, Ros A (2012) Transitioning streaming to trapping in DC insulator-based dielectrophoresis for biomolecules. Sens Actuators B Chem 173:668–675. doi:10.1016/j.snb.2012.07.080